JOURNAL OF EXPERIMENTAL AND THEORETICAL PHYSICS, 2024, Vol. 165, No. 2, pp. 159–183

ATOMS, MOLECULES, OPTICS

STRONG EXCITATION OF THE ELECTRONIC SUBSYSTEM OF GOLD BY AN ULTRASHORT LASER PULSE AND RELAXATION PROCESSES NEAR THE MELTING TEMPERATURE

© 2024 N.A. Inogamov [a,b,c*], V.A. Khokhlov[a,c], S.A. Romashevskiy[c], Yu.V. Petrov[a], M. A. Ovchinnikov[c], S. I. Ashitkov[c]

[a] *Landau Institute for Theoretical Physics of Russian Academy of Sciences* (*ITP*), *142432 Moscow Region*, *Chernogolovka*, *Russia*

[b] *The Federal State Unitary Enterprise Dukhov Automatics Research Institute* (*VNIIA*), *127055 Moscow*, *Russia*

[c] *Joint Institute for High Temperatures of Russian Academy of Sciences* (*JIHT*), *125412 Moscow*, *Russia*

**e-mail*: *nailinogamov@gmail.com*

Received September 15, 2023

Revised October 09, 2023

Accepted October 10, 2023

Abstract. Femtosecond lasers are widely used in scientific research and modern technologies. When applied to metals, ultrashort optical laser radiation produces a pronounced two-temperature state with hot electrons: $T_e >> T_i$, where T_e and T_i are the temperatures of the electron and lattice subsystems. Our experimental measurements were carried out using phase-sensitive (lock-in) detection technique on bulk and film (100 nm thick) gold targets. Due to the fact that in our experiments the repetition rate of heating (pump) pulses was reduced to 31 Hz, we were able to reach lattice temperatures near the melting point of gold. This occurs at the exit of the two-temperature stage in bulk targets. As we know, at the end of this stage, the temperatures converge, $T_e \approx T_i$. In bulk targets, at the highest fluences we achieved, the peak electron temperature increases to values around 20 kK. Theoretical calculations available in the literature give certain dependences for the electron-phonon coupling parameter α and the electron thermal conductivity coefficient k; they are the key parameters that characterize the two-temperature state. Our experiments showed that in the range of fluences with peak temperatures T_e above 10 kK and up to 20 kK, the measured values of α and k are significantly lower than than the values given by theories. Below this range of fluences, i.e., when the peak T_e is less than 10 kK, our measured values are in agreement with previous data. This is the first result of the paper. In addition, it is shown that at one-temperature stage, when the thermal energy stored in the electrons is very small, there is a significant influence of the fundamentally two-temperature coefficient α on heat transfer from the skin layer. This is due to the relatively small thickness of the heated layer, which is of the order of 200-300 nm in gold.

Keywords: *femtosecond lasers, electron-phonon coupling parameter, electron thermal conductivity, two-temperature state, gold*

DOI: 10.31857/S00444510240203e4

1. INTRODUCTION

Femtosecond (fs) laser systems are an indispensable research tool in science [1-4] and in materials processing technologies [5-9]. Accordingly, the interaction of fs radiation with matter has been studied on a broad front and for a long time [10-18]. Nevertheless, many problems remain relevant.

The physics of fs-impact is divided into two main parts (we will limit ourselves to the case of the optical excitation of metals). The first part studies the excitation of electrons in a condensed medium and the relaxation of excited states. The second part analyzes the subsequent phenomena occurring already in a thermodynamically equilibrium medium. On the one hand, the transition of condensed matter to a nonequilibrium state and relaxation to thermodynamic equilibrium are considered. On the other hand, the consequences of ultrafast heating already in equilibrium states are analyzed.

In turn, the first part is divided into two sections according to the degree of excitation. These are Knudsen and hydrodynamic flows. In the first (Knudsen's) section it is reasonable to refer to weak excitations, and in the second – to strong excitations (hydrodynamics). How do they differ? The difference between them lies in the relaxation time t_{e-e} of the electron subsystem. At weak excitation the time t_{e-e} exceeds the laser pulse duration τ_L and becomes comparable to the relaxation time t_{eq}.

We will limit ourselves to the case of gold and fs-pulses, when the time t_{eq} is units and tens of picoseconds and significantly exceeds the duration τ_L. At times smaller than the scale t_{e-e} the Fermi distribution in the electron subsystem has not yet been established [19, 20]. Several electron-electron collisions are required to establish the thermodynamic equilibrium of electrons. Weak excitations come from weak laser action because the free path time between electron-electron collisions, $t_{e-e} \propto 1 / T_e^2$ [21], decreases with the absorbed energy F_{abs}. The reason is that $t_{e-e} \propto 1 / E_e$ is due to the fact that $E_e \propto T_e^2$, where E_e is the electron energy.

Further in the text experiments and calculations with weak and sufficiently strong excitations will be presented. They refer to the Knudsen and hydrodynamic cases.

The situation at times $t < t_{e-e}$ should be described using the kinetic equation [19, 20]. In this case, the Knudsen number $Kn \sim 1$. The Kn number characterizes the transition from the nonequilibrium to the equilibrium case. It is equal to the ratio of the free path length to the characteristic spatial scale, $Kn = l_{mfp}/L$, or it is equal to the ratio of the mean free time to the characteristic temporal scale, $Kn = t_{mfp}/t_{eq}$. Working with the kinetic equation in a spatially inhomogeneous medium is complicated.

In the aerodynamics of rarefied air, the Chapman-Enskog method [22] was created to simplify the solution of the kinetic Boltzmann equation. This direction is associated with approximation of the kinetic Boltzmann equation in the form of expansion by powers of a small parameter, which is considered to be the number Kn. The first approximation by the Kn number is the Navier-Stokes equation. For the condensed medium with excited electrons, such analogs have not been created yet. In this kind of medium, there are approaches to the solution of the kinetic equation in the spatially homogeneous case (thin films) [19, 20].

The approach with separation into electronic (e) and ionic (i) subsystems [10, 23] leads to a significant simplification of solutions in the nonequilibrium case. In the equilibrium case, the thermodynamic system is characterized by one temperature. In the approach of the researches [10, 23] there are two temperatures – they are separate temperatures T_e and T_i for electrons and lattice – two-temperature (2T) approximation. The 2T approximation relies on the fact that the establishment of equilibrium between subsystems lasts longer than the establishment of equilibrium within e- and i- subsystems.

The 2T approach makes sense if the equilibration time in the electronic subsystem is small,

$$t_{e-e} \ll t_{eq}. \tag{1}$$

The equalization of temperatures T_e and T_i occurs in time t_{eq}. It is clear that the absorbed energy F_{abs} must be large enough to fulfill inequality (1). How large is large enough? Rough estimates give a threshold value of $F_{abs} \sim 1$ mJ/cm^2. Below in the paper we will clarify this position on the basis of experiments and calculations.

In our experiments and calculations, the gold target is at room temperature, i.e., heated above the Debye temperature of gold $\Theta = 170$ K before exposure. In thermodynamic equilibrium at $T > \Theta$, the main contribution to the lattice heat capacity is associated with phonon modes with wave vectors $k \sim k_D$ near the Brillouin zone boundary. We emphasize that in 2T states ($T_e \gg T_i$) almost the entire flux of energy transferred by electrons is directed to the same short-wavelength modes [24].

Let us replace the Brillouin zone by a sphere. The radius of this sphere in the wave vector space is $k_D = (6\pi^2 n_{at})^{1/3}$, where n_{at} is the concentration of atoms. The wavelength $\lambda_D = 2\pi / k_D = 0.2$ nm. The phonon-phonon interaction is due to anharmonicity of the crystal potential. Let us estimate the frequency ν_{p-p} of phonon-phonon collisions by lattice thermal conductivity:

$$\kappa_{lat} \sim (1/3)\, c_{lat}\, c_s^2 / \nu_{p-p}.$$

Hence $\nu_{p-p} \simeq 7 \cdot 10^{12} / \kappa_{lat}$ s^{-1}, where κ_{lat} is expressed in SI units. Accordingly, the phonon free path time $1/\nu_{p-p}$ between collisions is of the order of 100-200 fs at $\kappa_{lat} \sim 1$ W/K/m. The above estimate follows from molecular kinetic theory. In it, c_{lat} and c_s are the lattice heat capacity and the speed of sound, respectively. It is clear that many electron-electron and phonon-phonon collisions are required to thermalize the

far tail of the Fermi distribution and to thermalize the long-wavelength phonons, respectively. But the energy in both of these tails is small, so their filling is relatively insignificant.

Let us estimate the electron mean free path l_{mfp} in gold at room temperature. The length l_{mfp} is also called the ballistic length. The electron collision frequency, estimated using Drude's formula for electrical resistivity, is of the order of 10^{14} s^{-1}. At room temperature, the collision frequency is determined by phonon scattering. If the Fermi velocity is estimated as $v_F \sim 10^8$ cm/s, we obtain $l_{mfp} \sim 10^{-6}$cm ~ 10 nm, i.e., on the order of 30 interatomic spacings. As the electron and/or ion temperatures increase above room temperature, the collision frequency increases and the ballistic length decreases accordingly. In the Knudsen regime, the film thickness is of the order of the ballistic length.

Let us now talk about the experimental situation. Pump-probe technique allows for direct monitoring of the processes induced upon irradiation to fs pulses. [25]. In other words, it is the measurements of transient thermo reflectivity, TTR [26]. The principle is simple. Irradiation ("thermo") excites the electronic subsystem. As a result of the excitation, the optical characteristics change. Probing pulses are needed to determine the evolution (therefore "transient") in time of the changed optical characteristics, e.g., the variation of the reflection coefficient (reflectance evolution).

In the first works of the late 80s and early 90s, the energy of fs-lasers was weak [11-14], see also [27]. The irradiation (pump) caused such a small deviation from the room value that the probing signal was drowned in noise. Therefore, the measurements were performed in the mode of desired signal accumulation – the lock-in technique [12-14]. A sequence of N>>1 quadruple (two pairs each) laser pulses was applied to the target.

The first pair in the quadruple consisted of a skipped heating pulse (no pump pulse) and a diagnostic (probe) pulse. Thus, the first pair measured and memorized in the device memory the undisturbed value of the reflection coefficient R_0. The second pair, belonging to the same quadruple, had both the heating (pump) and diagnostic (probe) pulses. The changed value of the reflection coefficient R' was measured and memorized. In a series of N quadruples, the time difference between the heating and probing pulses t_{delay} and the amplitude of the heating pulse were strictly fixed. The amplitude of the probing pulse is negligibly small.

The variation ΔR of the reflection coefficient, $\Delta R = R' - R_0$, fluctuates due to noise. When the number of pulses $N \gg 1$ is large, the ΔR variation converges to the mean $\langle \Delta R \rangle$. In this case, the relative error decreases proportionally to $1/\sqrt{N}$.

In the following series, the time t_{delay} of the delay between the heating and probing signals was changed. Thus, the time evolution $\langle \Delta R \rangle (t_{delay})$ of the excited system after a heating pulse of fixed amplitude was determined [12-14, 28]. When the parameters of the heating pulse (amplitude, duration) change, the evolution changes.

The time interval t_4 ($t_4 \gg t_{delay}$) between consecutive quadruples must be long enough. This is necessary in order to guarantee cooling of the substance and return of the target to the initial state with a coefficient R_0 during the time t_4. Otherwise, the substance in the irradiation spot will degrade in the fatigue degradation regime [27, 29]. Fatigue degradation limits from above the amplitude of the heating (pump) pulse in the lock-in technique. It is clear that the cooling time t_4 after exposure to a pump pulse grows with the amplitude of this pulse.

As time went on, new laser systems were developed and the energy of the fs-action increased. With sufficiently powerful energy, it was possible to abandon the above complex lock-in mode with many repetitions (N>>1) of high stability pulses. The measured ΔR value began to be determined in one pair of heating (pump) and diagnostic (probe) pulses, since the ΔR value was rather large [25,30,31]. By varying the delay t_{delay} between pulses, the $\Delta R(t)$ dependence can be found. Note that a strong single impact irreversibly changes the characteristics of the target substance in the impact spot. Therefore, the next laser shot should be directed to a new, unexposed spot on the target surface.

A spectral interferometry technique was also developed, by means of which the $\Delta R(t)$ dependence is determined at once in one experiment with a single heating pulse [32,33]. In this case, a long (subnanosecond) frequency modulated diagnostic (probe) pulse is synchronized with a single heating fs-pulse, the different spectral components of which arrive at the target with different delay times t_{delay}.

Thus, the lock-in technique (II) and the single probing pulse technique (I) complement each other. With II it is possible to work with weak impulses when the accuracy of technique I is not sufficient. On the contrary, with I, one can remove the upper limit on the amplitude of the effect. As mentioned above, the limit is caused by degradation of the target due to damage accumulation and/or gradual accumulation of heat.

In the above experiments, heating and probing are performed by optical pulses. Sometimes they are harmonics of the fundamental frequency. For example, heating is carried out at the second harmonic, and probing is carried out at the first harmonic, see the example in [27]. There are more complicated schemes with time synchronization of arrival of different kinds of pulses on the target. Pump-probe studies with optical (pump) and non-optical (probe) pulses are carried out. With the help of soft X-rays, images are constructed of the dome development [34] during the separation (blistering) from the substrate of a thin film in the irradiation spot. Newton rings and interference fringe shifts [34] in laser beams at a wavelength of 13.9 nm are used for diagnosis. By diffraction on a time-varying crystal lattice, changes in the crystal structure as a result of fs-exposure are studied. In such studies, hard X-ray radiation [35] or an electron beam [36] is used for diffraction as a diagnostic (probe) pulse.

Let us return to purely optical pump-probe methods. The first studies of the specifics of the course of processes induced by fs-pulse, firstly, relied on lock-in apparatus and, secondly, aimed to describe electron-phonon relaxation [12-14]. Such relaxation lasts for picosecond(s). In this case, the illumination spot of the pump-pulse is much wider than the illumination spot of the probe-pulse. This is necessary to exclude inhomogeneity effects.

The real revolution took place in the late 1990s. First, as mentioned above, the energy of fs-lasers increased (so it was possible to exceed the nano-detachment threshold). Second, researchers when tracking of the processes initiated by fs-action, began to cover a much longer time interval (t_{delay} - up to units and tens of nanoseconds [30]; see also the work [37] on record observation durations). Third, the spot size of the probe-pulse became larger than that of the pump-pulse [30].

These three circumstances made it possible to observe Newton rings with an increasing number of rings in time. These circumstances are: exceeding the threshold; duration of observation sufficient for the detached shell to travel a path comparable to the wavelength of the probe-pulse; wide field of view of the probe-photograph covering the entire region of the detached shell.

The obtained data allowed us to declare a new (non-evaporation) character of flow generated by fs-impact [30, 38, 39]. It turned out that fs-impact leads to nano-detachment [38, 39] instead of the usual (for longer pulses) evaporative ablation. Equivalently, instead of the terms detachment or nucleation/cavitation, one speaks of thermomechanical ablation [38, 39] or stress confinement [40]. In early studies of electron-phonon relaxation [12-14], the hydrodynamic effects were negligible; in these studies, the lock-in technique was used, and the heats were weak, far below the threshold of thermomechanical ablation.

Let us conclude herewith the review on the physics of ultrashort laser impacts. The paper is organized as follows. In Sects. 2-7 the general view is presented. It is stated that at an early stage in bulk targets the cooling of the electronic subsystem in the skin layer is mainly due to the transfer of electronic energy from the skin layer by electronic heat conduction (Sects. 2-5). At this stage, the energy transfer from electrons to phonons plays a minor role (Sections 6 and 7).

In Sects. 8 and 9 present the experimental technique used and describe the main results. It is these results that served as a basis for the subsequent theoretical treatment. The point is that the TTR method presented above allows us to obtain experimental data for the relative change of the reflection coefficient $\Delta R(t)/R_0$ with time during and after ultrashort laser exposure. This is an indirect method: the $\Delta R(t)/R_0$ curve should be used to judge the state of the condensed medium with excited electrons. To convert the curve into parameters characterizing the system, it is necessary to have a numerical implementation of an adequate physical model.

Sects. 10 and 11 explain the physical techniques we used: the calculation of the heat transfer coefficient is given in Sect. 10, the optical model is given in Sect. 11. The final section summarizes the results of the work.

2. DOMINANCE OF ELECTRON HEAT CONDUCTIVITY IN BULK TARGETS

The data of lock-in measurements for film and bulk targets are presented in this paper. The comparison of TTR in the case of these two types of targets is shown in Fig. 1. In bulk targets at the 2T stage, the cooling of the electronic subsystem in the skin layer (i.e., the decrease of the surface temperature $T_e|_{surf}$) is mainly due to the transfer of electronic energy E_e from the skin layer to the volume by means of the electron heat flow

$$q = -\kappa \nabla T_e, \tag{2}$$

where κ is the heat transfer coefficient. At this stage, the energy transfer E_e to the phonon subsystem

has little effect on the rate of temperature decrease T_e in the skin layer.

On the contrary, in the film the flux (2) is suppressed geometrically due to the ultra-small film thickness – in our experiments the film thickness is equal to $d_f = 100$ nm. Cooling in such a film is associated with energy transfer from the electronic subsystem (energy E_e) to the ionic subsystem (energy E_i). Specific (per unit volume) power

$$\dot{E}_{ei} = \dot{E}_e - \dot{E}_i$$

of energy exchange between these subsystems is equal (usually in units of W/m^3)

$$\dot{E}_{ei} = \alpha(T_e - T_i),$$

where α is the electron-phonon exchange coefficient.

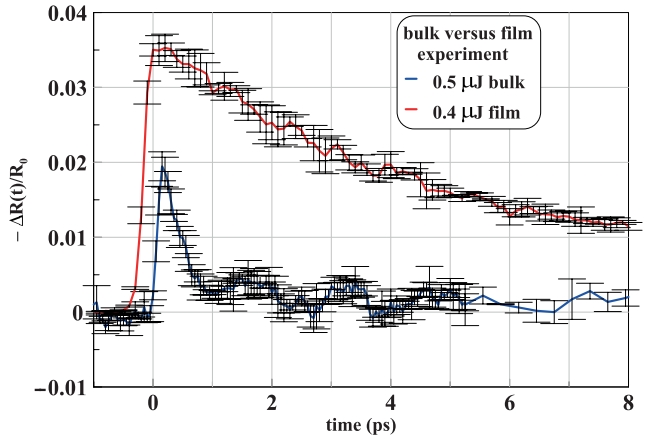

Fig. 1. (In color online) Comparison of TTR (i.e., $\Delta R/R_0$) in film and bulk targets; $\Delta R = R(t) - R_0$, R_0 is the value of the reflection coefficient of a probe-pulse with $\lambda = 800$ nm at room temperature. The energies of the corresponding laser pump-pulses are indicated (see Sect. 8 for a description of our experiments). In the film and in the bulk target, the mechanisms of the decrease in the surface electron temperature $T_e|_{surf}$ are different. In the film, the decrease of $T_e|_{surf}$ (and consequently TTR) is due to exchange (3), whereas in the bulk target cooling due to electron heat flux (2) dominates, see explanations in the text.

Let us give estimates explaining the situation shown in Fig. 1. Conversion of the pump-pulse energy (indicated in the box in Fig. 1 in μJ) first into the incident radiation fluence F_{inc}, and then into the absorbed energy F_{abs}, gives values F_{abs}, equal to 3.4 mJ/cm^2 for the film and 3.7 mJ/cm^2 for the bulk target. In our experiments, the amount of reflected pump-pulse energy is measured. From these measurements, the absorption coefficient A at a pump-pulse wavelength of 400 nm at an angle of 45° under p-polarization is obtained to be 0.7 and 0.8 for the volume and film, respectively. Hence the given values of F_{abs} follow. Note that for the 45° angle, the literature data for A range from 0.7 to 0.75, see https://refractiveindex.info/. Note that the thickness of the gold film (100 nm) is such that the radiation energy that has passed through the film can be neglected.

If we distribute the absorbed energy $F_{abs} = 3.4$ mJ/cm^2 in the electron subsystem at a thickness of $d_f = 100$ nm, the electrons will heat from room temperature $T_{rt} = 293$ K to 3600 K. In the calculation, it is assumed that the increment of the specific electron energy is equal to

$$E_e = \frac{\gamma}{2}(T_e - T_{rt})^2 = \frac{F_{abs}}{d_f}.$$

According to the Fermi gas theory for gold, the coefficient $\gamma = 63$ J/K^2 /m^3.

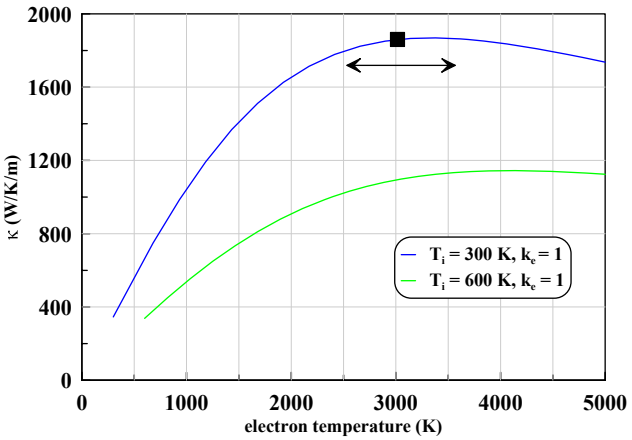

Fig. 2. (In color online) Dependences of the thermal conductivity coefficient κ of gold in the solid phase at a normal density of 19.3 g/cm^3 on the temperatures T_e and T_i. To evaluate (4), we assume that the heating of the ionic subsystem in the surface layer is small, i.e., $T_i \approx 300$ K. The average value of $\kappa \approx 1900$ W/K/m over the segment of T_e temperature variation from 3600 to 2600 K. The specified segment of T_e temperatures is highlighted by a two-sided horizontal arrow. The description of the model for the κ coefficient calculation is given in Sect. 10.

In a volumetric target, the estimate of the energy per unit area carried by the heat flux from the surface layer with thickness $d_f = 100$ nm for time t_{cool}, has the form

$$Q_{ehc} = (\kappa \Delta T_e / d_f) t_{cool}. \quad (4)$$

Here the index "ehc" means electron heat conduction. For the estimation it is necessary to take the values κ, ΔT_e and t_{cool}, which refer to the experimental situation shown in Fig. 1. We are interested in the case of a bulk target, represented by the blue curve in Fig. 1.

Let us take the temperature difference $T_e|_{surf}$ in expression (4) from the maximum temperature, equal to about 3600 K, to a temperature $\sqrt{2}$ times lower. In this case, the electronic energy E_e of the layer will decrease by a factor of two, since $E_e \propto T_e^2$. At the 2T stage, the amplitude of the TTR signal $\Delta R(t)/R_0$ is approximately proportional to $(T_e|_{surf})^2$. Therefore, we take the time interval at half-height of the peak of the blue curve in Fig. 1 as the cooling time of the electronic subsystem t_{cool}. This corresponds to about 500 fs.

The indicated surface temperature difference is marked by a horizontal segment in Fig. 2. In the estimation (4) we substitute $\kappa \approx 1900$ W/K/m. The heat transfer coefficient κ in the theory developed by us is composed of electron-electron and electron-ion (phonon scattering) contributions. The coefficient κ is shown in Fig. 2. We choose the electron-electron contribution to κ according to [41]. The electron-phonon contribution is calculated according to [42].

Substituting the accepted values $\kappa \approx 1900$ W/K/m, $\Delta T_e = 1000$ K and $t_{cool} = 0.5$ ps into expression (4), we obtain $Q_{ehc} = 1$ mJ/cm^2, i.e. during the time t_{cool} the electron carries away heat flux (2) from the surface layer into the volume more than a quarter of the absorbed energy $F_{abs} = 3.7$ mJ/cm^2.

The strongest electronic cooling due to thermal conductivity significantly reduces the peak value of TTR in Fig. 1 already at the pump-pulse energy absorption time interval. In our experiments, the pump-pulse duration was quite significant: 150-200 fs. This circumstance explains the difference in the height of the TTR peaks of the bulk and film targets in Fig. 1.

Now let us estimate the cooling rate of the electronic subsystem of the film with thickness $d_f = 100$ nm. The corresponding TTR dependence is shown by the red curve in Fig. 1. This estimation will allow us to determine the value of the electron-phonon exchange coefficient α in formula (3).

According to formula (3) we write down

$$\Delta E_{ei} = \alpha T_e d_f t_{cool-film}. \quad (5)$$

In (5), the magnitude of ΔE_{ei} gives the decrease in energy stored in the film during the film cooling time $t_{cool-film}$. The value of ΔE_{ei} refers to the unit area of the film. The reduction is due to the transfer of energy to the lattice subsystem. In (5), we neglect the ionic temperature T_i in the temperature difference from formula (3).

Let us take the commonly accepted value of the electron-phonon exchange coefficient

$$\alpha = 0.2 \cdot 10^{17}\ \text{W/K/m}^3. \quad (6)$$

This value corresponds to the value of the electron-phonon exchange coefficient for gold at low heating. Let us take as T_e in (5) the average temperature of 3100 K at the temperature decrease interval from 3600 to 2600 K. These temperatures are determined from the law of conservation of energy in terms of absorbed energy and the Fermi expression for the electron energy density, see above. According to the red curve on Fig. 1, the duration of the time interval at the half-height of the peak is approximately 4.5 ps. Let us take this time as the cooling time $t_{cool-film}$ in expression (5). Substituting these values into expression (5), we find that $\Delta E_{ei} = 2.8$ mJ/cm^2. This value is approximately equal to the energy absorbed by the film of 3.4 mJ/cm^2.

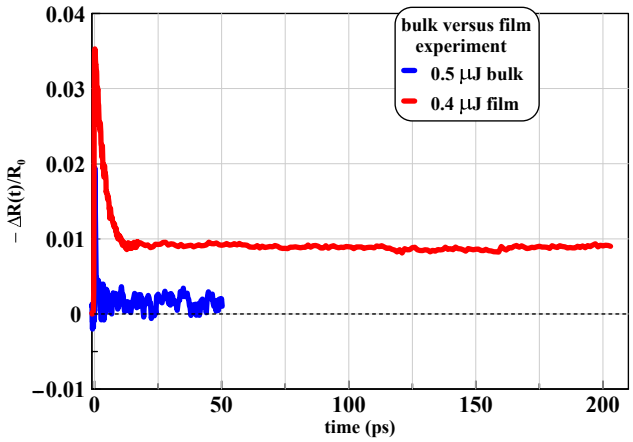

Fig. 3. (In color online) The dashed horizontal line corresponds to $\Delta R = 0$, i.e., the return of the reflection coefficient of the probe-pulse to the room value. As we can see, the film temperature is about 4-5 times higher than the surface temperature of the bulk target. The point is that the film is deposited on a glass substrate. The thermal conductivity of glass is much less than that of gold. We judge the temperature by ΔR, since in the one-temperature (1T) stage the deviation of ΔR is approximately proportional to the temperature. The experiments by means of which the curves are obtained TTR are described in Sects. 8 and 9.

For our film with $d_f = 100$ nm, the absorbed energy $F_{abs}|_{lim} = 3.4$ mJ/cm^2 is limiting, i.e., it is not possible to perform TTR measurements at values of F_{abs}, exceeding this limit. This is due to the lack of heat dissipation into the volume that cools the absorbing surface. In Fig. 3 shows the time extended (compared to Fig. 1) TTR dependences. It is clear that an ultrathin film on glass cools in the time interval t_4 between pump-pulses much less than a bulk gold target; the thermal conductivity of glass is two orders of magnitude lower than that of gold. Therefore, the limit $F_{abs}|_{lim} \approx 60$ mJ/cm^2 is much higher for the bulk target.

Thus, unfortunately, it is not possible to compare TTR on film and bulk targets at higher heating $F_{abs} > 3.4$ mJ/cm^2, as is done in Fig. 1. In the energy range $3.4 < F_{abs}$ [mJ/cm^2] < 60, we will have to limit ourselves to the data obtained on bulk targets.

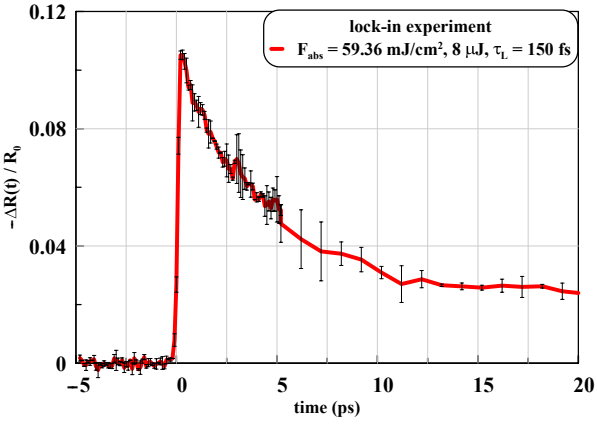

Fig. 4. The same as in Fig. 3 for the bulk target, but at an absorbed energy F_{abs} 16 times greater. A scheme illustrating the relationship between the time dependences of the pump-pulse intensity $I(t)$ and TTR is presented in Fig. 5.

The two main conclusions with which to conclude this section are as follows.

First, in bulk targets at the 2T stage, the cooling of the skin layer is mainly due to electronic heat conduction.

Second, the theoretical values for the coefficients κ (see Fig. 2) and α (6) are suitable for describing the experiment. It will be shown below that at absorbed energies higher than about 30 mJ/cm^2 the theoretical values of these coefficients become unsuitable for describing the experiments.

From the further presentation it will be clear that the thesis about the determining role of the electron heat flux is preserved at strong heating. This takes place for the case of a bulk target, for the 2T stage and for the case when the energy is significantly higher than the limit $F_{abs} = 3.4$ mJ/cm^2 of "burn-through" of a 100 nm thick gold film.

3. DETERMINING ROLE OF ELECTRONIC THERMAL CONDUCTIVITY

Fig. 4 shows the initial part (full observation lasted up to 350 ps) of the experimental TTR dependence for the bulk target. The data are collected at the "burn-in" limit for the bulk target. It was possible to obtain these results at a record value of absorbed energy F_{abs}. The record was achieved due to the ultra-low frequency of $1/t_4 = 31$ Hz pulse repetition in the lock-in technique, see Sec. 1.

The maximum of the TTR dependence in Fig. 4 is shifted relative to the maximum of the intensity time course

$$I(t) \approx I_0 \exp(-t^2/\tau_L^2)$$

approximately to the region of the inflection of the Gaussian approximation on the descending wing of the Gaussian function, see Fig. 5. With poor heat conduction and a small value of the coefficient α defined in formula (3), the point M in Fig. 5 shifts to the right relative to the point $t = 0$, down the descending wing. Conversely, with fast heat dissipation and slow input of laser energy into the absorption layer (skin layer), the point M shifts to the left. The section from the beginning of irradiation to the TTR maximum is labeled with number *1* in Fig. 5.

Estimates and numerical simulations with the 2T-hydrodynamic code show that the decline of the electronic surface temperature $T_e|_{surf}$ and TTR in section *2* of Fig. 5 is mainly due to electronic heat conduction. In this respect, the strong-heating case considered here is not different from the weak-heating case discussed in Sect. 2.

Gradually, as TTR and temperature $T_e|_{surf}$ decrease, the rates of surface cooling due to thermal conduction κ and due to heat transfer into the lattice α are compared. This occurs in the final section *3* of the 2T stage in Fig. 5. In this transition from the 2T stage to the one-temperature (1T) stage (when $T_e \approx T_i$), $T_e|_{surf}$ is still significantly higher than $T_i|_{surf}$.

Nominally, section 4 in Fig. 5 is a 1T heat flow section, since locally in the target volume the temperatures $T_e(x,t)$ and $T_i(x,t)$ are approximately equal. In fact, the 2T effect is latently present here. Now the temperature $T_e|_{surf}$ is slightly smaller than the

temperature $T_i|_{surf}$. This condition ensures that surface cooling continues in the 1T stage. As will be shown below, only the correct choice of the purely 2T coefficient α ensures the correct time course of the surface temperature decrease, and hence of the TTR at section 4. Therefore, section 4 is called the latent 2T-part (latent presence of α).

In this section, we will mainly analyze section *2* in Fig. 5. It is necessary to understand how the spatial propagation of the incoming radiation and the radiation energy that has already entered the skin layer occurs. Let us repeat the estimates used in Sect. 2 for small radiation fluxes. These estimates are based on the law of conservation of energy, the heat conduction equation and the equation describing the energy exchange between electron and ion subsystems.

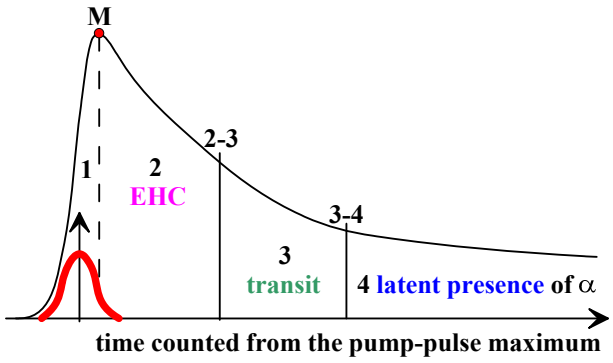

Fig. 5. (In color online) Pump-pulse is shown by a red bump, its maximum is reached at time $t = 0$. This scheme explains the characteristic *1-2-3-4* sections of the TTR time dependence (black curve) and the synchronization of pump-pulse and TTR in time (EHC – electron heat conduction).

Let us write the law of conservation of energy in the form

$$\frac{\gamma}{2}T_e^2 = \frac{F_{abs}}{d}.$$

Hence

$$T_e = \sqrt{2F_{abs} / d\gamma}.$$

For strong heating, we can neglect the initial room temperature T_{rt} and write T_e^2 instead of $(T_e - T_{rt})^2$. We fix the energy $F_{abs} = 59.36$ mJ/cm^2 and take $\gamma = 120$ J/K^2/m^3. We have increased the effective value of the coefficient γ compared to the value following from the Fermi gas theory. This is necessary in order to account for the increase in the electronic heat capacity due to the connection of the electrons for gold $5d^{10}6s^1$ d-zone at values of T_e greater than 5 kK [17,43]. We normalize the thickness of the layer accepting radiation energy as $d = d_{20} \cdot 20$ nm, where d_{20} is a dimensionless ratio. As will be seen, the thermal conductivity κ is strongly suppressed at high temperatures T_e. Therefore, we chose the value of 20 nm instead of 100 nm at weak heating, see Sect. 2. Substituting the above values, we obtain

$$T_e = 22/\sqrt{d_{20}}, \tag{7}$$

where the temperature T_e is given in kiloKelvins. The estimate (7) agrees with the data of numerical simulations by 2T-hydrocode. These data will be summarized below.

Let us repeat the estimate (4) for the heat flux carrying the absorbed radiation energy through the electron subsystem from the layer d. Let us replace in this estimation the film thickness d_f by the thickness 20 d_{20} nm and substitute the temperature (7) instead of the temperature ΔT_e. As a result, we obtain

$$Q_{ehc} = \kappa\sqrt{2F_{abs}/d^3\gamma}\, t_{cool} = \\ = 1.1 \cdot 10^{14}\, \kappa_{1000}\, t_{cool}/d_{20}^{3/2}\ \text{mJ/cm}^2. \tag{8}$$

Here t_{cool} is the cooling time of layer d due to the action of electronic heat conduction, which is given in seconds. The heat conduction coefficient $\kappa = 1000$ is written as $\kappa = 1000\kappa_{1000}$ W/K/m. Cooling is due to the transfer of energy into the volume by heat conduction.

Let's see what cooling time t^*_{cool} would be needed to carry all the absorbed energy $F_{abs} = 59.36$ mJ/cm^2 out of layer d. According to this, we write

$$Q_{ehc} = F_{abs},$$

where the energy Q_{ehc} is given by expression (8). Hence, we obtain

$$t^*_{cool} = (1/\kappa)\sqrt{F_{abs}\, d^3\gamma/2} = \\ = 0.53 d_{20}^{3/2}/\kappa_{1000}\ \text{ps}. \tag{9}$$

According to the estimation (9), a significant decrease in the thermal conductivity coefficient κ is required to slow down the energy removal from the surface layer to 5-7 ps. The time of 5-7 ps corresponds to the TTR decay time in the experimental dependence in Fig. 4.

4. HEAT FLOW

In Sect. 3 estimates of the energy (8) transferred to the volume due to heat conduction were given. Fig. 6 shows the instantaneous estimated profiles (not an estimate) of the flux $q(x,t = 0)$ (2) obtained by integration of the 2T equations; the system of equations is derived in [44, 45]. Similar equations are applied in [46]. As we can see, the pump-pulse intensity I_0 far (26 times) exceeds the electron heat flux $q(x = 20$ nm, $t = 0) = 8.6 \cdot 10^9$ W/cm^2; this is the flux at point b in Fig. 6. The maximum radiation intensity $I_0 = 2.23 \cdot 10^{11}$ W/cm^2 corresponds to the red circle in Fig. 6. Therefore, the duration of surface cooling significantly exceeds pump-pulse duration τ_L.

The segments *ab* and *cd* are plotted in Fig. 6 to justify the choice of the characteristic thickness of the surface layer $d = 20$ nm adopted in the evaluations in Sect. 3. It is possible to choose d even smaller, but it is not reasonable to choose larger thicknesses, since the flux at point b is $8.6 \cdot 10^9$ W/cm2, and the flux variation (segment *cd*) at the interval $20 < x < 40$ nm is $1.6 \cdot 10^9$ W/cm^2, i.e., 5 times smaller. The flux maximum q (2) is located at a depth of about 10 nm.

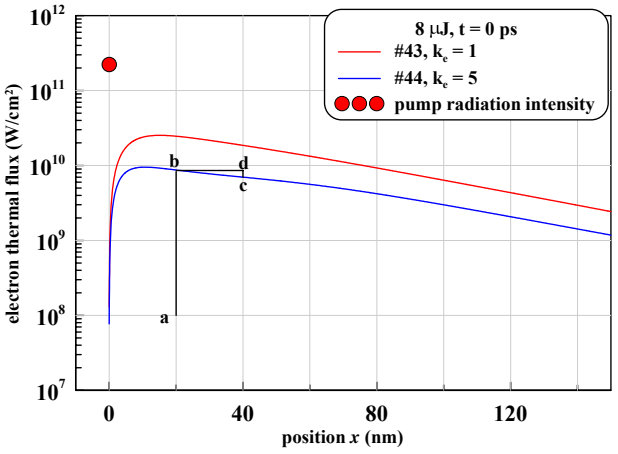

Fig. 6. (In color online) Flux distribution (2) over space at time $t = 0$, when the maximum intensity $I_0 = n^{-1/2}F_{abs}/\tau_L$ of the absorbed radiation flux $I(t)$ *is* reached; $\tau_L = 150$ fs. This maximum is marked by the red circle above. The blue curve refers to the case with a fivefold (k_e factor) enhancement of the contribution to the thermal resistance due to electron-electron scattering, see Sec. 5.

In calculations 43 and 44, shown in Fig. 6, the 2T-hydrodynamic code was applied without considering hydrodynamic motion: velocity $u(x, t) \equiv 0$, see [44, 45]. A comparison of calculations 42 (with hydrodynamics) and 43 (stationary medium) is shown in Fig. 7-9. The response of TTR to the pump-pulse impact is determined by the evolution of the surface parameters: $T_e(t)|_{surf}$, $T_i(t)|_{surf}$ and gold density $\rho(t)|_{surf}$. As we can see, the time course of surface temperatures is only weakly affected by the presence of the material motion, see Fig. 7. The gold density at the surface is lower by 2-3% in the case when the motion is taken into account, see Fig. 8. These differences have little effect on the TTR dependence. Consequently, at absorbed energies from 60 mJ/cm^2 and below, hydrodynamics can be disregarded when calculating TTR. An energy of 60 mJ/cm^2 is about a quarter of the energy relative to the ablation threshold; the description of such high fluences requires a separate study.

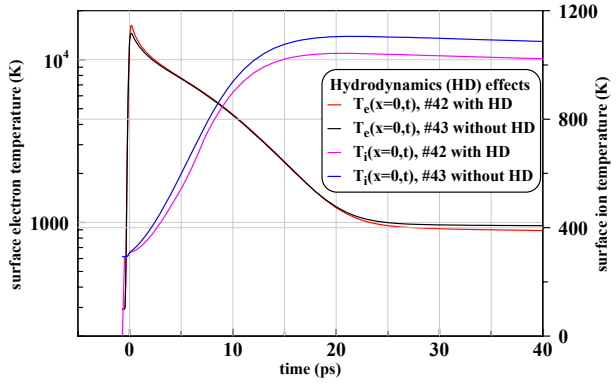

Fig. 7. (In color online) Time dependences of electronic $T_e(t)|_{surf}$ and ionic $T_i(t)|_{surf}$ surface temperatures. The results of numerical simulations with the same values of the initial parameters are compared. The difference is that in calculation 42 the full system of hydrodynamic equations is integrated, see [44, 45], while in calculation 43 only thermal equations are left in the system.

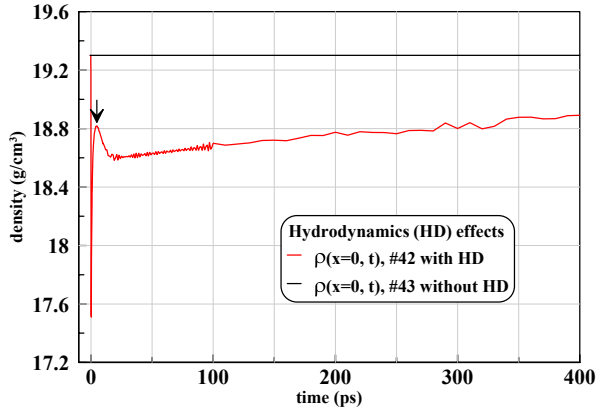

Fig. 8. (In color online) Time dependence of gold density on the surface $\rho(t)|_{surf}$. The calculation 42, hydrodynamics (red curve) is taken into account. Therefore, due to heating, expansion occurs (see displacement Δ in Fig. 9) and the density decreases. In calculation 43 there is no motion: $u \equiv 0$. Consequently, the density of the bulk target is homogeneous and equal to the initial density.

Of course, hydrodynamics cannot be neglected near the ablation threshold.

As mentioned above, in our energy range F_{abs} the TTR signal is only weakly affected by the material motion in the target. However, there is a curious detail. This acoustic propagation into the target thickness of the trace from a short-term increase in the electron pressure p_e at the initial segment 2T-stage. This trace in the form of a curve sharp kink can be clearly seen in Fig. 9. The electronic pressure p_e is accounted for in the 2T equation of state, which is necessary to solve the full system of 2T-hydro-dynamics equations [44, 45]. The equation of state is taken from quantum mechanical calculations of photoexcited gold, see [17].

The sharp density change in Fig. 8 is associated with the kink in Fig. 9. The coordinate of the maximum in Fig. 8 is 5.2 ps. The maximum is marked with an arrow. The duration of the density fall down from the point of the pump-pulse action until the point of 5.2 ps is due to the action of the pressure p_e. This time correlates with the decline time of the TTR signal. In Fig. 4, the width of the TTR peak at its half-height is equal to 5-7 ps.

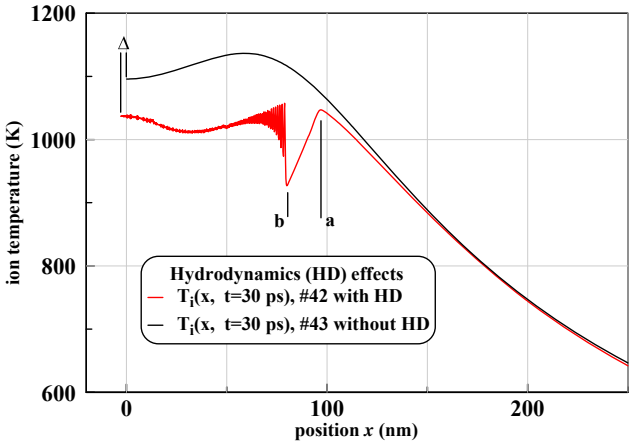

Fig. 9. (In color online) Instantaneous spatial profiles of ionic temperature at point of 30 ps. The effect of motion on the profile is analyzed. Due to the motion, there is a displacement of the boundary by a segment Δ. The bright spike on the red curve is due to a sharp increase in the electron pressure p_e due to the effect of the pump-pulse.

5. HEAT TRANSFER COEFFICIENT

Fig. 6 shows two instantaneous dependences of the electronic heat flux distribution $q(x,t)$ (2). They refer to different dependences of the thermal conductivity coefficient $\kappa(T_e, T_i, \rho)$. As discussed above, the coefficient κ was calculated theoretically. The coefficient κ was found by adding the thermal resistances,

$$s = 1 / \kappa, \quad s = k_e s_{ee} + s_{ei}.$$

The resistance s_{ee} was calculated using the physical model proposed in [41] for aluminum, with modification of this model for the case of gold. The work [41] is based on the solution of the kinetic equation in the tau approximation. The resistance s_{ee} arises due to electron-electron scattering. The electron-phonon contribution $\kappa_{ei} = 1/s_{ei}$ was taken according to [42] for gold in 2T states.

We need the weighting factor k_e in order to harmonize the calculated and experimental results. The theory corresponds to the value $k_e = 1$. Fig. 10 shows the dependencies related to the red and blue curves in Fig. 6. The red curve in Fig. 6 refers to the upper group of three curves in Fig. 10. The blue curve respectively refers to the lower group.

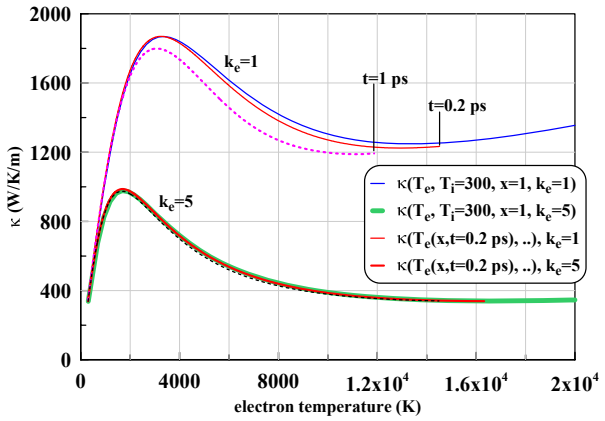

Fig. 10. (In color online) Theoretical dependences of the thermal conductivity coefficient κ on the temperature T_e at fixed temperature T_i = 300 K and density (shown by thin blue and thick green curves). These curves are depicted over the T_e temperature range up to 20 kK. The thick and thin red curves show the instantaneous profiles of the κ coefficient at the time point of 0.2 ps for calculations number 43 and 44, respectively. The termination point of the profile, marked by the vertical line, corresponds to the maximum T_e temperature on the profile at the instantaneous time. As time passes, the temperature at the maximum decreases. The maximum is reached at the boundary. The time point of 0.2 ps corresponds to the highest T_e temperature of the surface. The dashed curves refer to the profiles at the time point of 1 ps.

The lower group of three curves in Fig. 10 represents the case with a rather strongly suppressed electronic contribution to the thermal conductivity. This is achieved by increasing the multiplier k_e. Increasing k_e leads to an increase in the thermal resistance due to the electron-electron interaction. At the same time, the thermal conductivity coefficient κ decreases. The dependences of the coefficient κ on the electron temperature T_e are shown in Fig. 10 in the temperature

range up to 20 kK by the blue solid and green solid curves. The temperature dependences T_e are shown at a fixed ionic temperature $T_i = 300$ K and at a fixed density. The density is equal to the density of gold ρ_0 under normal conditions. The value $x = \rho/\rho_0$ is equal to the density normalized by the density ρ_0 (the density ratio thus denoted should not be confused with the coordinate). On the graphs (blue and green curves) in Fig. 10 we have $x = 1$.

At room conditions, the thermal conductivity of gold is $\kappa = 318$ W/K/m. The theory reproduces this value. The blue and green dependences in Fig. 10 start from it. Under 1T conditions, the value of κ depends weakly on temperature up to the melting temperature; as is known, after melting the coefficient κ decreases in 2-3 times. The weak dependence of the coefficient κ of solid gold on temperature is due to the fact that the growth of the frequency ν_{ei} of electron-phonon collisions is compensated by the growth of the heat capacity of electrons – heat carriers. At low temperatures, the frequency of electron-phonon interactions dominates over the frequency ν_{ee} of electron-electron collisions.

It is clear that if we fix the temperature T_i and increase the temperature T_e, the coefficient κ will increase. This is due to the partial removal of electron degeneracy and the growth of heat capacity on this basis at a fixed frequency of electron-phonon collisions $\nu_{ei} \propto T_i$. This part of the 2T-heat conductivity dependence κ (T_e, T_i, ρ) corresponds to the growth of the blue and green curves in Fig. 10.

At further increase of temperature T_e, the frequency ν_{ee} becomes equal to the frequency ν_{ei}, and then begins to exceed it. For rough estimates, it can be assumed that the frequency ν_{ee} grows in proportion to the square of the temperature T_e. The exact dependence deviates from the law $\nu_{ee} \propto T_e^2$, see [41]. Because of this, the linear growth of the coefficient κ with increasing temperature T_e at a fixed temperature T_i stops. This cessation of growth occurs at about $T_e \approx 3.2$ kK for the blue curve and $T_e \approx 1.8$ kK for the green curve, see Fig. 10.

In numerical modeling, the theoretical formula for the coefficient κ was put into the code. In calculation 43 (44), the coefficient κ with the value $k_e = 1$ ($k_e = 5$) was used. The results of calculations 43 and 44 are compared in Fig. 6 and 10. The functions $T_e(x, t)$ and $T_i(x, t)$ are found in the calculation. From these, other functions are determined, such as the heat flux $q(x, t)$ (2), see Fig. 6, or the heat transfer power $\dot{E}_{ei}$ (3).

Let us take from the calculation the instantaneous profile of the heat transfer coefficient $\kappa(x, t = t_{fix})$ on the spatial variable x. Let us also take from the calculation the profile of the electronic temperature $T_e(x, t = t_{fix})$ at the same point of time t_{fix}. We exclude the argument x from this pair of functions. As a result, we obtain the dependence $\kappa(T_e, t = t_{fix})$ at point of time t_{fix}.

Just such parametric profiles at times 0.2 and 1 ps are shown in Fig. 10. One pair of profiles at times 0.2 and 1 ps refers to calculation 43, the other pair – to calculation 44. At the selected time instants, the ion temperature has not had time to change appreciably from the initial temperature; the initial temperature (i.e., before irradiation) was the room temperature. It is clear, therefore, that the indicated profiles are close to the temperature dependence of the thermal conductivity coefficient at ionic temperature $T_i = 300$ K, adopted in calculations 43 or 44 (choice of the coefficient k_e).

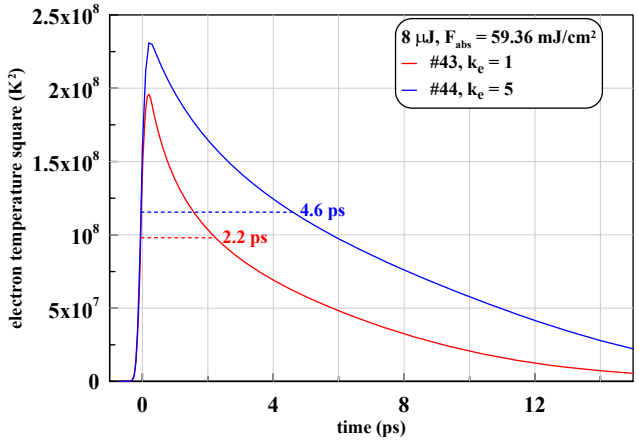

Fig. 11. (In color online) Time dependences of the surface electron temperature square T_e. It can be seen that the heat flux limitation broadens the peak of the temperature squared to approximately match the experimental results in Fig. 4. The blue curve refers to calculation 44 with suppressed ($k_e = 5$) heat transfer coefficient κ.

As the time t_{fix} increases, the parametric profiles in Fig. 10 depart from the temperature dependence of the thermal conductivity coefficient κ at ionic temperature $T_i = 300$ K. This is due to the increase in ionic temperature at the profile $T_i(x, t = t_{fix})$ compared to the value of 300 K. The solid parametric curves refer to the time moment of 0.2 ps. The thin red curve is obtained from calculation 43, the thick red curve from calculation 44. The curves shown by the small dashes represent the 1 ps moment. The crimson dashes are calculation 43 and the black dashes are calculation 44. In calculation 44, the temperature T_i increases more slowly. Therefore, the separation between the parametric profile on the one hand and the dependence of the

thermal conductivity coefficient on the electronic temperature on the other hand is slow. If the ionic temperature on the profile remained equal to 300 K, there would be no separation of these curves.

The main findings of this section are as follows.

First, electron heat flux q dominates as a cooling mechanism of the skin layer at energies $F_{abs} \approx 60$ mJ/cm^2. These are energies on the order of a quarter of the ablation threshold and slightly below the melting threshold.

Second, the flux q fails to cope with the transfer into the volume of absorbed radiation flux of energy I, see Fig. 6. In this regard, at the indicated energies and pulse durations, the cooling time of the skin layer significantly exceeds the duration of the laser pump-pulse.

Third, only with a significant limitation of the heat flux can we achieve in theory a significant broadening of the TTR peak (decrease in the rate of energy release from the skin layer) corresponding to the experiment. On this basis, the choice in the heat conduction model is made in favor of the multiplier $k_e = 5$. Accordingly, we choose the blue curve in Fig. 6.

To substantiate the third conclusion, we give Fig. 11. It is clear that a decrease in the electron heat flux will slow down the rate of decline of the electron temperature at an early stage, when the absorbed energy is concentrated almost entirely in the electron subsystem. How will this affect the TTR signal? Obviously, the TTR peak will become broader, see Fig. 4. The optical model data will be summarized below. Here we will limit ourselves to an estimation. We consider that the shape of the TTR signal in the upper part is determined by the electron-electron scattering frequency ν_{ee}. For a rough estimate, we can assume that the frequency $\nu_{ee} \propto T_e|^2_{surf}$. Accordingly, the time course of the square of the temperature T_e at the surface is plotted in Fig. 11.

6. ELECTRON-PHONON INTERACTION

The transfer of energy from the electron subsystem to the ionic subsystem plays an important role. The corresponding specific power is given by formula (3). The energy balance equation of the electron subsystem has the form [44, 45]

$$\rho_0 \frac{\partial (E_e/\rho)}{\partial t} = -\frac{\partial q}{\partial x^0} - \dot{E}_{ei} + \frac{\rho_0}{\rho} Q - p_e \frac{\partial u}{\partial x^0}. \quad (10)$$

There are three main acting terms in the right part of the equation. These are electron thermal conduction (2), electron-phonon thermal interaction (3), and a short-range ($\tau_l = 150$ fs) source of absorbed laser energy Q. The fourth summand is related to the mechanical work. Under the conditions under consideration, it is small, see the explanations on this matter in Fig. 7-9.

At the very initial stage there is an intense outbreak – the Q member dominates, see Fig. 6. Next, after some time, there is the stage of dominance of the first term (electron heat conduction, EHC – electron heat conduction), see the scheme in Fig. 5. Finally, at the end of the 2T-stage and throughout of the further the 1T stage, the second (2) and third (3) members are of the same order become relevant and complement each other in heat transport in the metal at relatively low temperatures. At this stage, heat transport is carried out by electrons, and energy release or storage occurs in the lattice subsystem, which heat capacity is much greater at these temperatures than the electron heat capacity.

The 2T-hydrodynamic code uses a one-dimensional x-axis partitioning scheme into Lagrangian nodes, see [44, 45]. Of course, the one-dimensional approach is justified because the size of the illumination spot on the surface (from units to thousands of micrometers) by an optical laser is larger than the fs impulse heating depth (fractions of a micrometer, see Fig. 6, 9). In expression (10), the variable x^0 is the Lagrangian coordinate, ρ_0 is the density of gold under normal conditions. Before the pump-pulse impact, the target is homogeneous and its density is equal to ρ_0.

In numerical calculations we used approximation of the coefficient α of the following form

$$\alpha(T_e,\rho) = 0.2 \frac{1 + (T_e/5060)^2}{1 + (T_e/7050)^5} \left(\frac{\rho}{\rho_0} \right)^{5/3}. \quad (11)$$

In formula (11), the value of α is given in units of 10^{17} W/K/m^3. This approximation takes into account the data of [27] on determining the dependence of the exchange coefficient α (3), (11) on the electronic temperature.

A comparison of energy losses in the skin layer due to heat conduction (2) and due to lattice heating (3) is shown in Fig. 12 and 13. The heat flux q (2) and the specific (per unit volume) power of heat exchange between subsystems (3) are different in physical meaning and dimensionality. We are interested in the cooling of a surface layer with a thickness of the order of the skin layer thickness. The thickness of this surface layer is taken as $d = 20$ nm, see Sec. 3 and formula (7). Fig. 12 and 13 compare the heat flux $q(x = 20$ nm, $t)$ and the value E_{20} (12).

Fig. 12 and 13 show the heat flux $q(x = 20$ nm, $t)$, which removes electron energy from layer d through the right boundary of this layer. This is so because the vacuum boundary (the left boundary of layer d) is thermally insulated: on it the indicated flux is zero, see Fig. 6. Thus, the flux q cools the layer d. Another important source of change in the internal energy of the electron subsystem centered in layer d is the energy exchange between the subsystems, E_{20}. This quantity is defined as the integral of the drain (or inflow) of energy into the electron subsystem.

$$E_{20}(t) = \int_0^d \dot{E}_{ei}(x,t)dx. \qquad (12)$$

Here the integrand is given by formula (3). The sign of E_{20} depends on the sign of the temperature difference in formula (3).

At the span 1 in the scheme in Fig. 5, the absorbed energy is pumped into the electron subsystem of layer d for the time $\tau_L = 150$ fs. In the variant of the experiment considered here, this energy is equal to 59.36 mJ/cm^2. At the absorption span 1, the radiation flux (intensity I) far exceeds the cooling electron heat flux q, see Fig. 6. Therefore, the electronic temperature of the surface increases dramatically. At the span 2, the decrease of the electronic temperature is mainly due to the action of the flux q, see Fig. 12 and 13. Moreover, as follows from Fig. 11, when describing the heat transfer coefficient at temperatures $T_e = 10 - 18$ kK, we should use not our theoretical curve with $k_e = 1$, see Fig. 10 and 11, but a dependence with a strongly suppressed coefficient κ (parameter $k_e = 5$), see the discussion in Sec. 5 and Fig. 11. The span 3 in the scheme in Fig. 5 is transitional between 2T and 1T stages. At the 1T stage, the temperatures $T_e(x, t)$ and $T_i(x, t)$ are locally approximately the same. The analog of Fig. 7 for calculation 44 gives a value of 31 ps for the transition termination time (i.e., the end of the span 3). At about this time, the sharp decrease in the electronic temperature $T_e|_{surf}(t)$ at the surface is replaced by a slow decrease in the temperature $T_e|_{surf}(t)$. The calculation 43 in Fig. 7 corresponds to this moment with a value of 22 ps. The moment of the end of the transition span 3 is shown by segment 3-4 in Fig. 5. The beginning of the segment 3 in Fig. 5, it is natural to put the time of about 10 ps, when the fluxes $q(x = 20$ nm, $t)$ and $E_{20}(t)$ (12) converge, see Fig. 12 and 13.

At the end of the span 3, the electron surface temperature becomes less than the ion surface temperature. This is a significant moment. For calculations

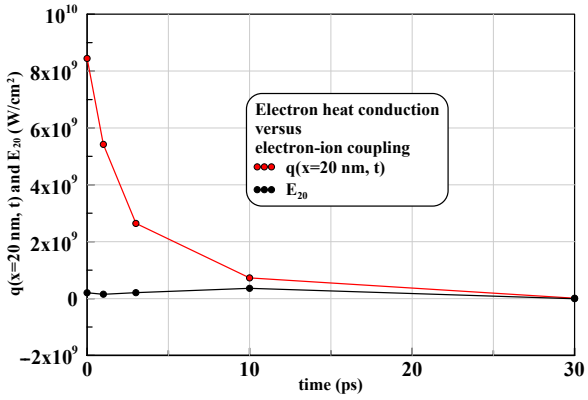

Fig. 12. (In color online) Comparison of energy fluxes. The flux $q(x = 20$ nm, $t)$ takes out the energy of the electron subsystem from the surface layer of thickness d. The flux E_{20} (12) removes (or adds) energy to the electron subsystem belonging to the layer d. The information following from the numerical calculation shown here is illustrated by sections 2, 3, and 4 in the schematic in Fig. 5. At the span 2 (the pronounced 2T stage), the flux q dominates. Then at the subsequent span 3, the fluxes q and E_{20} converge. At span 4, these fluxes are approximately equal in absolute values.

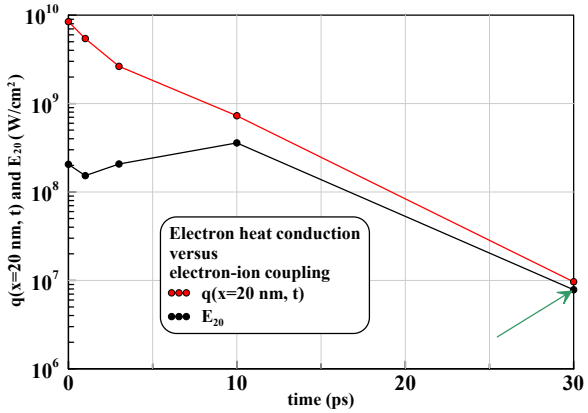

Fig. 13. (In color online) This figure repeats the previous one, but with a logarithmic vertical axis. We see that at the 2T stage the flux q exceeds the flux E_{20} associated with the exchange between the electron and phonon subsystems. At the 1T stage these fluxes are approximately the same. The green arrow on the right indicates the value of the flux E_{20} at the time point of 30 ps. At this moment, the flux E_{20} has a negative sign. In this figure, we have replaced this sign with a positive sign so that we can use the logarithm axis. So, after the transition from $T_e|_{surf} > T_i|_{surf}$ to $T_e|_{surf} < T_i|_{surf}$, the fluxes q and E_{20} have different signs. At the same time, they are approximately equal in absolute value and thus compensate each other.

43 and 44, this occurs at the time points of 21 and 26 ps, respectively. Further, the energy accumulated exactly in the ionic subsystem is removed from the surface layer d by the flux q into the volume.

Until this significant moment, the flux q was withdrawing the energy E_e of the electronic subsystem. The energy E_e was small and still decreased due to the flux q (and due to the flux E_{20} too, of course). At the same

time, the energy of the ionic subsystem E_i was increasing due to the influx (12) —the E_{20} flux had a plus sign. After the change of the sign of the surface temperature difference, the accumulated energy E_i begins to decrease. At the end of the span 3, the energy E_e is negligibly small compared to the energy E_i. This is due to the huge difference of heat capacities of subsystems at low temperatures.

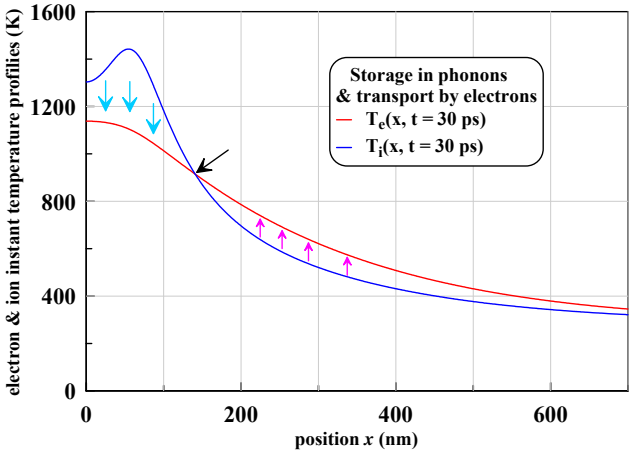

Fig. 14. (In color online) Illustration of the phonon and electron subsystems working together to transfer heat from a hot region to a cold region. Phonons with large heat capacity play the role of heat storage and light, fast electrons carry out the heat transfer, see the text. The length of the computational span is gradually increased. This is necessary to exclude the influence of the right boundary, which is far away in the target thickness. At 30 ps, the right boundary is at a distance of 2 μm.

At the span 4, the energy E_i of the surface layer d decreases. During the time interval dt, a small portion dE_i of the energy E_i is transferred to the electronic subsystem, since $T_e < T_i$, see (3). This portion is then withdrawn from the layer d by the electron flux q in the specified time interval. Note that the difference in surface temperatures $T_i - T_e$ is significant in magnitude. At $t = 50$ ps this difference is 200 K (approximately 20% of the temperature T_e). Gradually the temperature difference $T_i - T_e$ decreases: at $t = 400$ ps it is equal to 80 K (10% of the temperature T_e). The condition $T_i > T_e$ on the surface temperature ensures the continuation of surface cooling at the 1T stage. It is natural to call this phenomenon the hidden presence of 2T effects at the nominally 1T stage.

At the time point of 30 ps, the change of sign of the $T_i - T_e$ difference as a function of the x coordinate occurs at $x = 142$ nm. This point is marked by an oblique black arrow in Fig. 14. Thus, at $x < 142$ nm the energy dE_i is withdrawn from the hotter ion subsystem and

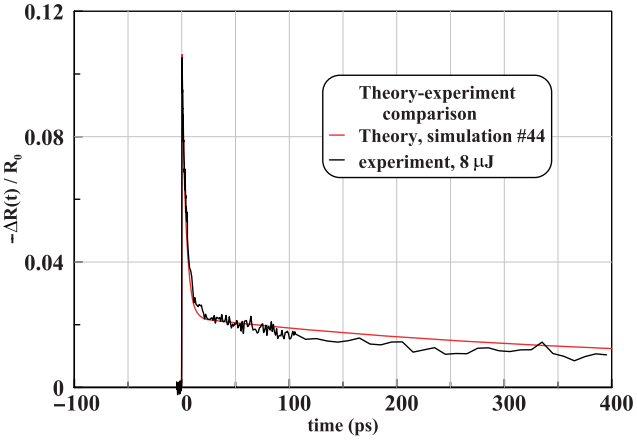

Fig. 15. (In color online) Comparison of calculation 44 with experiment. The absorbed energy F_{abs} is taken, as in the present experiment with laser pump-pulse energy of 8 μJ and energy $F_{abs} = 59.36$ mJ/cm^2. The red curve is the calculation, black is the experiment in the lock-in technique. The optical model, according to which the recalculation of the time dependences of T_e, T_i, ρ at the surface into TTR is described below in Sect. 11.

at $x > 142$ nm, on the contrary, it is transferred to the cooler ion subsystem, see Fig. 14. In Fig. 14, the blue downward arrows at $x < 142$ nm illustrate the energy transfer from phonons (they are hotter) to electrons, i.e. phonon cooling occurs. On the contrary, the pink upward arrows at the half-axis 142 nm $<x<\infty$ indicate heating of phonons on this half-axis. A similar effect in the lateral temperature-diffusion expansion of the heating spot was recently summarized in [47]. It was called "negative thermal conductivity" there. In fact, it is a conventional heat conduction mechanism acting under 1T conditions. At the point $x = 142$ nm there is a inflection point in the instantaneous profile of the electronic temperature. As time passes, the point of change of sign of the $T_i - T_e$ difference moves deeper and deeper into the target thickness. In this case, the local temperature difference related to the local temperature becomes smaller and smaller.

We conclude this section by saying that the analysis of the fluxes q and E_{20} shown in Fig. 12 and 13 allowed us to further understand the physical meaning of sections 2, 3, and 4 in Fig. 5.

7. COMPARISON OF THEORY AND EXPERIMENTS

Fig. 15 and 16 compare theoretical and experimental TTR, i.e., functions from time $\Delta R(t)/R_0$, where $\Delta R = R(t) - R_0$, R_0 is the reflection coefficient of a gold target at normal incidence of an electromagnetic wave (probe) with a wavelength of 800 nm under normal conditions: temperature of 293 K, pressure

is equal to 1 atm. Note that in the lock-in technique the change in reflection coefficient ΔR is determined, not the reflection coefficient R. In Fig. 15 and 16, the time is counted from the maximum of the pump pulse.

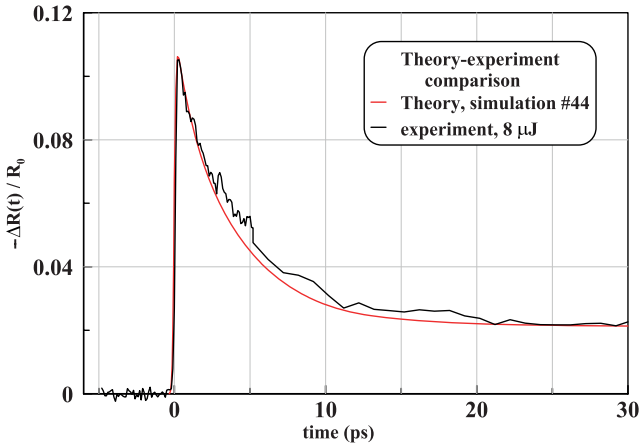

Fig. 16. (Online in color) The 2T stage is shown in detail and the 1T stage transition region. Colors are same as in Fig. 15.

The dependences in Fig. 15 and 16 are clearly divided into stages of fast and slow decline of the TTR signal. The first stage consists of the span 1, 2 and 3 – sharp rise and fast decline of the TTR amplitude, see the definitions of the plots in Fig. 5. The second stage is the span 4. The separation of the stages takes place at point 3-4 in Fig. 5. At the plot 4, the TTR amplitude continues to decline, but at a much slower rate. A discussion of the physical mechanisms of heating and cooling was devoted to Sec. 6.

It is important to note that using the developed model (description of parameters κ and α) it was possible to describe the span 4 with slow decay of the TTR amplitude. In our previous article on this topic [27], the slow decay was absent: the TTR amplitude reached a constant value at the span 4, whereas experiment indicated a decrease in TTR, see Fig. 5 in [27].

In the present work, it was found that the absence of attenuation in the paper [27] was due to the choice of approximation for the parameter α. In the paper [27], the dependence from the papers [48, 49] was chosen as the dependence $\alpha(T_e)$ for gold. The approximation of this dependence has the form [49]

$$\alpha = \left(0.2 + \frac{(T_e\,|_{eV})^{3.6}}{1 + (T_e\,|_{eV})^{3.5} + 0.9(T_e\,|_{eV})^{4.1}}\right) \times \left(\frac{\rho}{\rho_0}\right)^{5/3}. \quad (13)$$

The values $\alpha(T_e, \rho)$ in formula (13) are given in units of 10^{17} W/K/m^3. The electron temperature $T_e|_{eV}$ is taken in eV units.

Dependences $\alpha(T_e, \rho = \rho_0)$ are presented in Fig. 17. In the present work, the dependence (11) is used in numerical modeling. In [27], formula (13) was used. In order that at energies $F_{abs} > 30$ mJ/cm^2 to match the experiment on the rate of TTR decline at the 2T stage, it was necessary to reduce the heat transfer coefficient κ at high temperatures T_e using the factor k_e. If the values of α were left at the relatively high level given by formula (13), the ionic temperature at the transition to the 1T stage was obtained too high and did not correspond to the experiment. Therefore, it was necessary to decrease the values of α in order to allow the weak thermal conductivity κ to heat the layer of sufficient thickness and thus reduce the surface temperature T_i.

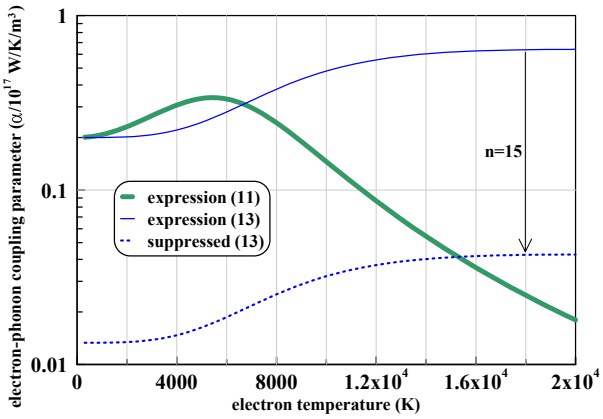

Fig. 17. (In color online) Dependence of the electron-phonon interaction parameter α on electron temperature at normal density $\rho = \rho_0$.

To reduce the value of α, the function (13) was divided by the suppression factor $n > 1$ in [27]. An example of a weak electron-phonon interaction is shown in Fig. 17 by the blue dashed curve. This curve is obtained by dividing function (13) by the suppression factor $n = 15$. In order to slow down the rate of TTR decrease and lower the T_i temperature at the transition from the 2T stage to the 1T stage, in [27], the factors k_e and n were chosen large enough: k_e up to 7.5, n up to 30.

In this way, it was possible to bring both the rate of decrease of TTR at the 2T stage in agreement with experience and the temperature T_i at the end of the 2T stage down to the experimental measurements. The only problem was the too slow decrease of the calculated temperature $T_i(t)|_{surf}$ at the 1T stage.

In the present work, this difficulty has been overcome. The point is that the suppression factor acted on the coefficient α uniformly over the whole temperature range T_e. Including the values of α were lower than the experimentally determined values (6) at relatively low temperatures $T_e < 4$-5 kK. It would seem that in 1T states the parameter α becomes unimportant – heat transfer is determined by the coefficient κ. Moreover, the coefficient κ in our heat conduction model tends to the reference values of $\kappa \approx 300$ W/K/m in the solid phase when aspiring to the 1T state, see Sec. 10. It turns out that both coefficients are essential for heat transfer in 1T states.

Our calculations in this paper have shown that the values of α at relatively low temperatures at the 1T stage determine the temperature difference between T_e and T_i, see Sect. 6, where it is written about the spans 3 and 4. Thus the values of α affect the heat transfer from the surface to the volume at 1T the span 4. The rate of temperature decrease $T_i(t)|_{surf}$ on the surface depends on this heat transfer.

In turn, the TTR amplitude depends on the temperature $T_i(t)|_{surf}$, especially in the 3rd and 4th stans in Fig. 5; see Sec. 11 on the optical model. In the approach adopted here, the values of α are given by formula (11). The corresponding dependence is shown in Fig. 17 by the green curve. As can be seen, this curve, firstly, has low values of α at high temperatures T_e and, secondly, comes out to the experimental values of α (6) at low temperatures T_e. The values of α (6) were obtained in the now old papers [11-14] when the heats in lock-in techniques were weak.

Let us make a small digression related to the modern development of the mentioned works.

(a) In [11-14], firstly, the value of α (6) was confirmed, and secondly, it was shown that at low temperatures T_e the coefficient κ in 2T states is high – the diffusivity χ is two orders of magnitude higher than the tabulated values under normal conditions. The works [12-14] were characterized by the first applications of the lock-in technique on ultrathin gold films and weak heating of the electron subsystem – temperatures T_e not more than about 1 kK, fluences $F_{abs} \sim 1$ mJ/cm^2 and less. We note recent works [50-52] with the same parameters of very weak pump-impact on ultra-thin films. They consider the lateral propagation (spatial broadening on the surface) of the electron temperature profile of the $T_e|_{surf}(y, z, t)$ surface with time. Here y, z are coordinates on the irradiated surface of the film. The index "$|_{surf}$" means that the surface temperature is considered. The surface is the $x = 0$ plane. Positive values of the x coordinate refer to gold, see Fig. 6, 9. The optical probe-pulse cannot look deeper into the thickness of gold than the skin layer. The decision is to study the evolution of the $T_e|_{surf}(r, t)$ profile on the surface; we consider the pump-pulse spot on the surface as a circle, then the radius r is counted from the center of the circle. This is done in [50-52]. It turns out that the evolution of the diffusion of electron thermal energy laterally (along the surface of the ultrathin film) is similar to the diffusion in depth.

(b) The results of recent works [50-52] essentially repeat the conclusion made earlier in [12-14] and [53]. This conclusion is as follows. The thermal diffusivity $\chi = \kappa/c$ of gold is much higher at the 2T stage ($\chi \sim 100$ cm^2/s) than at the 1T stage ($\chi \approx 1$ cm^2/s). The 2011 paper [53] provides a simple explanation. It is shown that this is due to the weak coupling of the electron subsystem (it has a small heat capacity c) with the ionic subsystem (large heat capacity $3k_B$). The weak interaction of the subsystems takes place at the 2T stage. The weakness of the thermal interaction between the subsystems compared to the electronic heat transport is stated here (see Fig. 12 on this point). Another conclusion of the articles [50-52] concerns the determination of the α coefficient. Both old and new papers conclude that this coefficient is equal to the value (6). We emphasize that this value refers specifically to weak heating, see Fig. 17.

(c) The reversal of the electron heat flux in films from the direction normal to the film to the direction along the film was considered earlier in [54] (Section 3.2 on cooling), [55] (Section 2), and [56]. It was shown that the thermal broadening Δr_T at the 2T stage along the film surface is approximately equal to the thickness of the heating layer $d_T \approx 2\sqrt{\chi t_{2T}}$ of the target in depth at the 2T stage. Substituting the temperature diffusivity $\chi = 100$ cm^2/s increased at the 2T stage into the estimate of d_T and taking the duration of the 2T stage t_{2T} in picoseconds, we obtain $d_T \approx 200\sqrt{t_{2T}}$ nm. The broadening Δr_T is the increase in the radius of the R_L pump-pulse irradiation spot on the target surface. It is clear that for the success of measurements of the broadening Δr_T as a function of time, first, the R_L spot must be small (less than a micrometer) so that the scales of R_L and Δr_T are comparable. Second, the spot must have a sharp edge at which the intensity distribution along the radius decreases sharply.

(d) The Liu formula [57] is often used in experiments to determine the threshold and, secondly, on the basis of the slope r^2 dependence on the logarithm of the laser pulse energy ln E_L to determine the laser beam radius on the irradiated surface. Here r is the radius of the damage spot. Of course, for the method

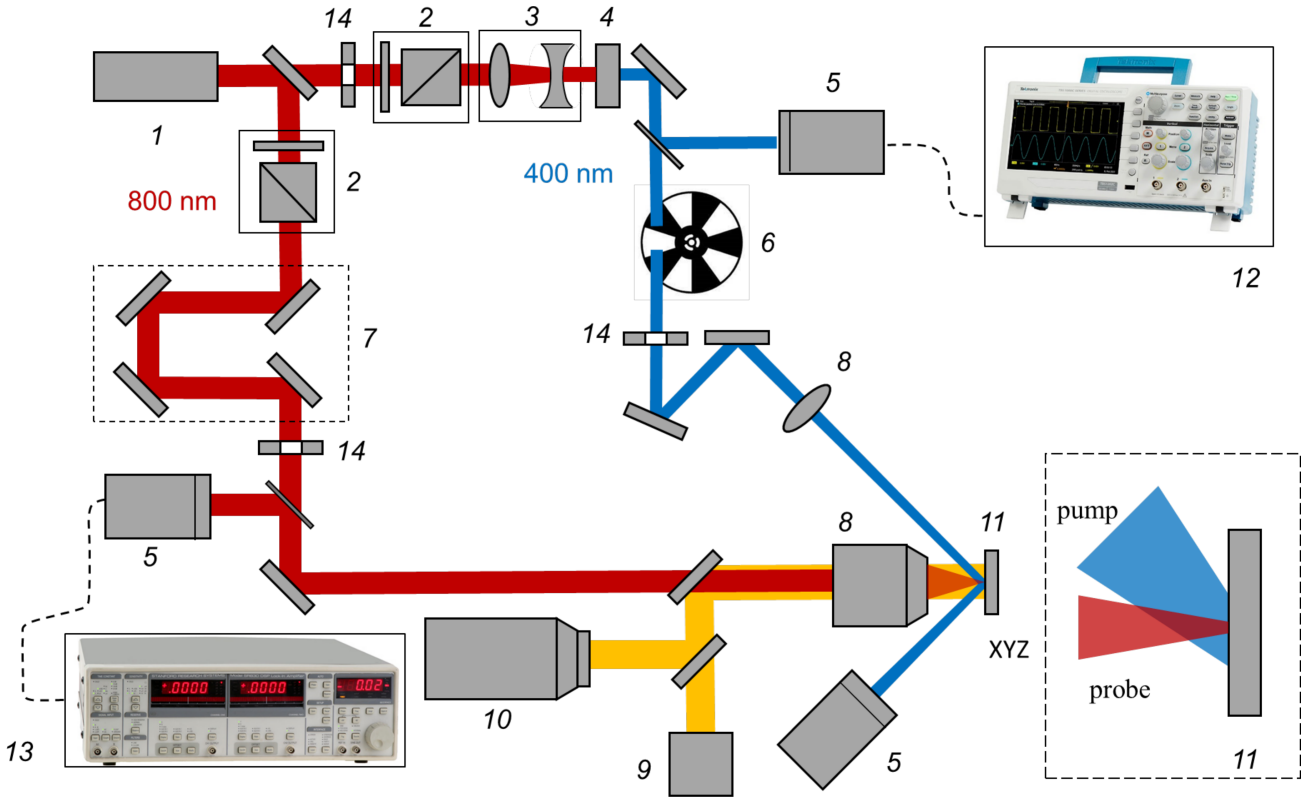

Fig. 18. Experimental scheme: *1* – laser; *2* – attenuator; *3* – telescope; *4* – BBO second harmonic crystal; *5* – photodiode; *6* – mechanical interrupter (chopper); *7* – optical delay line; *8* – focusing lens; *9* – backlight lamp; *10* – CCD camera; *11* – experimental sample; *12* – oscilloscope; *13* – synchronous amplifier; *14* – apertures.

of the work [57], the radial intensity distribution over the surface must be a Gaussian function. It is clear that the rapid thermal broadening of the heating spot will violate the dependence taken from [57], see [58].

To conclude this section, we can say that the approach we have developed allows us to describe the experiment satisfactorily, see Figures 15 and 16.

8. EXPERIMENT

The experimental measurements were carried out using a pump-probe technique (Fig. 18) using a regeneratively amplified femtosecond laser with a repetition rate up to 1 kHz, and a phase-sensitive detection technique using a lock-in amplifier and an optical modulator (chopper) [59].

Polycrystalline bulk gold sample was used as experimental sample *11*. In another series of experiments, a polycrystalline gold film with a thickness of 100 nm on a glass substrate was used. The film thickness was measured using an atomic force microscope (Veeco, Multimode V).

The source of radiation *1* was a femtosecond titanium-sapphire laser system (Legend, Coherent, USA) with pulse parameters: wavelength $\lambda_l = 800$ nm, duration $\tau_L = 60$ fs, energy E up to 1.1 mJ. A Pockels cell was installed at the output of the regenerative amplifier to improve the contrast of the laser pulse.

The probe pulse repetition rate was varied from 63 Hz to 1 kHz. The reference frequency for the lock-in amplifier was set by a Thorlabs MC2000B mechanical chopper with MC1F60 disk *6*, which decreased the repetition rate of the pump pulses to 31.5 – 500 Hz. Lock-in detection was performed with a filter slope of 24 dB/octave and a time constant of 100 ms. The equivalent noise bandwidth (ENBW) was 0.78 Hz and the waiting time was 1000 ms. The in-phase component X at the output of the lock-in amplifier was recorded with a Tektronix TDS 3054C oscilloscope *12* and software controlling the position of the motorized optical delay line.

The heating pulse of laser radiation was converted in the β-barium borate (BBO) crystal *4* into the second harmonic with a wavelength of 400 nm and an energy up to 25 μJ. To vary the energy of heating and probing

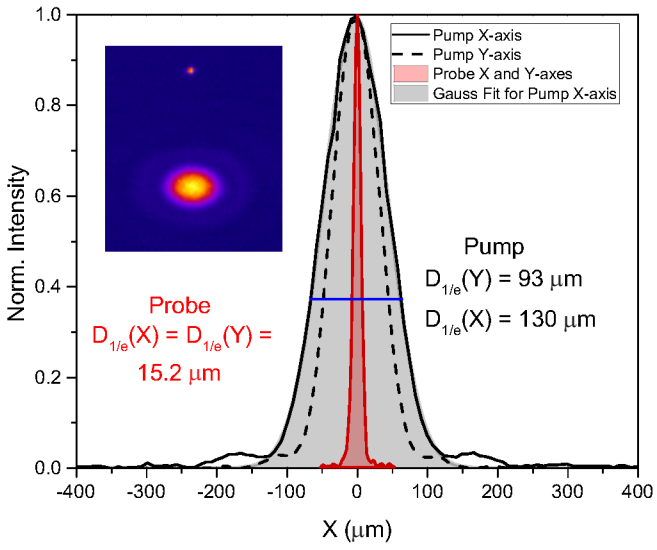

Fig. 19. (In color online) Spatial distribution of heating and probing radiation: for the heating pulse, the X- and Y-axis distribution is shown; for the probing pulse, the distribution is uniform in the X- and Y-axes; the Gaussian function approximation is given for the heating pulse in the X-axis; inset shows the distribution of heating (large spot at the bottom) and probing (small spot at the top) radiation in focus on the target, measured with a CCD camera. The blue horizontal line indicates the level of 1/*e* with respect to the maximum.

pulses, attenuators *2* consisting of a half-wave plate and a polarizer (Glan prism) were used. The probing radiation energy was controlled by a Thorlabs DET100 A/M photodiode *5*. The heating (pump) energy was measured by a calibrated photodiode *5* and varied from 0.4 to 8 μJ in the experiment.

The radiation of the heating pulse of *p*-polarization at wavelength of 400 nm was focused on the sample at an angle of 45°, and the radiation of the probing pulse at wavelength of 800 nm was focused normally to the sample's surface.

Fig. 19 shows the distribution profile of the intensity of heating and probing pulses on the target, recorded by PCO Sensicam QE CCD camera *10*.

The spatial distribution of the heating radiation corresponded to a Gaussian distribution with radii r_{0x} = 65 μm and r_{0y} = 46.5 μm at the 1/*e* level. The magnitude of the energy density of the heating pulse incident on the target was calculated using the formula

$$F_0 = \frac{E}{\pi r_{0x} r_{0y}}.$$

Here F_0 is the energy density at the center of the focal spot, E is the pulse energy measured by the photodiode. The incident energy density on the target varied in the range from 5.3 to 84.8 mJ/cm^2. The energy density measurement error did not exceed ±3%. The value of the experimentally measured reflection coefficient of heating radiation was 0.3 for the bulk sample and 0.2 for the gold film.

The spot radius of the probing radiation (7.6 μm in 1/*e* level) was significantly smaller than the heating radiation (see Fig. 19), and the energy density did not exceed 0.08 mJ/cm^2.

To change the time delay between the heating and probing pulses, we used an optical delay line *7* consisting of two mirrors and a Thorlabs LTS300/M motorized translator, which allows moving the reflector with an accuracy of 1 μm, see Fig. 18. The specified accuracy corresponds to a time delay step of 6.6 fs. The ultimate time resolution in this case is determined by the probe pulse duration and is about 60 fs. The sample under investigation was placed on a motorized three-axis translator. Motorized tables from Standa with a stroke length of 10 mm were used in this case.

The probing signal reflected from the target was monitored by photodiode *5* and fed to the lock-in amplifier input of the Stanford research systems SR830 *13*, which has a dynamic range of 100 dB. Backlight *9* and CCD camera *10* were used to visualize the target surface and spatial alignment of heating and probing radiation.

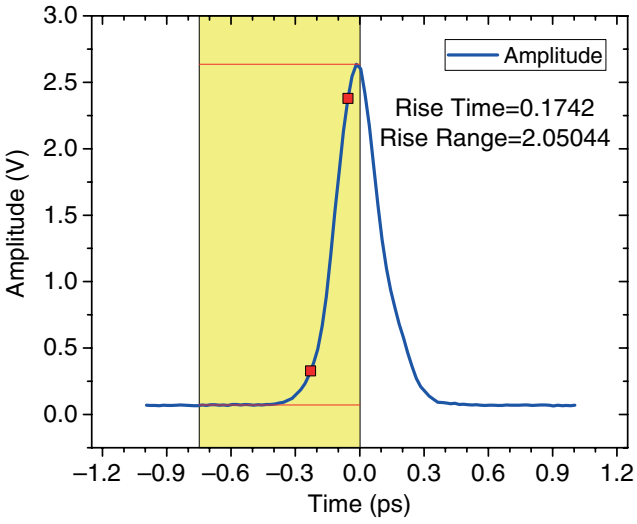

Fig. 20. Cross-correlation function of heating and probing pulses in the target plane.

To synchronize the heating and probing beams, a BBO third harmonic generation crystal was placed in the target plane, and after it a holographic diffraction grating of 300 strokes/mm was placed for spectral selection of radiation at wavelength of 266 nm. The

third harmonic radiation was detected by a photodiode. By moving the delay line translator, the cross-correlation function (Fig. 20) of the heating and probing pulses was obtained. The position of the delay line corresponding to the maximum of the third harmonic signal was taken as the "zero" delay. In this case, the maximum of the heating pulse maximum coincides in time with the probing pulse maximum. After determining the "zero" delay, the sample under investigation was placed and the time dynamics of the reflection coefficient was measured.

The duration of the probing pulse measured by the autocorrelator was 60 fs. The duration of convolution of heating and probing pulses was 244 fs (at FWHM).

To determine the value of R_0, the probing radiation signal was recorded at a frequency of 1 kHz in the absence of heating and modulation of the heating radiation. After that, the value of $\Delta R/R_0$ was determined. The amplitude measurement error was determined as the value of the standard deviation when averaging over several measurements. This error exceeded the value of the instrument error and was no more than $2 \cdot 10^{-4}$.

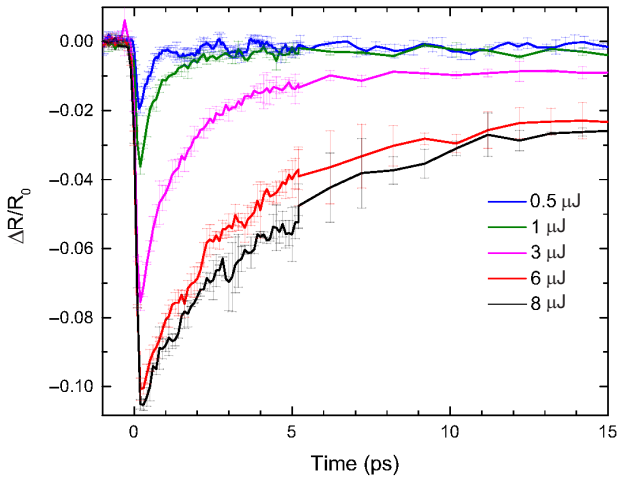

Fig. 21. (In color online) Time dependences of the TTR signal of a bulk gold target at different laser pulse energies in the 0-15 ps time interval.

9. EXPERIMENTAL RESULTS

In the experiment, measurements of the relative change of the target reflection coefficient, $\Delta R/R_0$, as a function of time were carried out with subpicosecond resolution at different energy densities of heating pulses. The delay line used allowed us to record time dependences of the TTR signal with a step of 6 fs. The scanning delay step was varied depending on the rate of change of the TTR signal and ranged from 30 fs at early times (0-10 ps) to 10 ps at later times (100-350 ps). The probing radiation was focused to the center of the heating region. Experimental dependences were obtained up to the maximum possible energy density of heating pulses, which does not lead to irreversible changes associated with degradation of the target surface. For this purpose, measurements were carried out at the minimum repetition rate of heating pulses of 31.5 Hz.

Figure 21 shows the TTR signal dependences of the bulk gold target at different fs-pulse energies.

For each value of laser pulse energy, three series of scans were performed with subsequent averaging of the obtained time dependences. The error was determined by the standard deviation of these measurements.

The table shows the the correlation between the incident laser pulse energy, incident energy density and absorbed energy density for the measured reflection coefficient of heating radiation from a bulk gold target equal to 0.3.

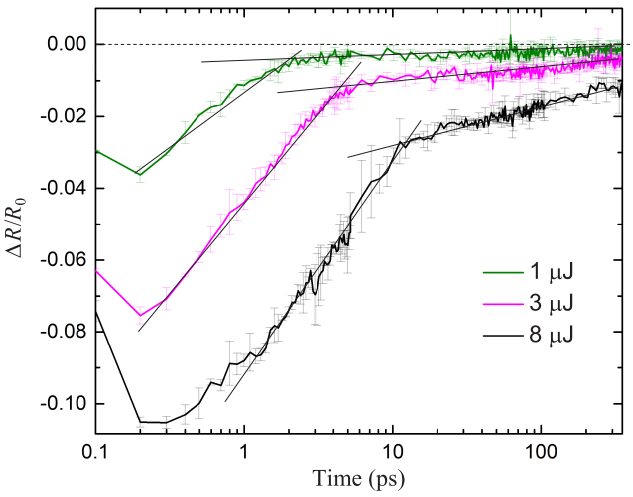

Fig. 22. (In color online) Time dependences of the TTR signal of the bulk target at different fs-im pulse energies in the time interval of 0-300 ps. The time scale is given in logarithmic scale.

Table. Parameters of the heating pulses on the targets

No.	E, μJ	F, mJ/cm^2	F_{abs}, mJ/cm^2
1	0.5	5.3	3.7
2	1	10.6	7.42
3	3	31.8	22.26
4	6	63.6	44.52
5	8	84.8	59.36

It follows from the above dependences that with increasing fs-pulse energy the TTR signal decay time increases and ranges at the $1/e$ level from 0.5 ps at 0.5 μJ to 7 ps at 8 μJ.

Fig. 22 shows the dependences of the TTR signal for three values of laser fs-pulse energy in a wide time interval.

Each of the plots shows two characteristic time intervals with different rates of decrease of $\Delta R/R_0$, which obviously characterize the dynamics of cooling of the gold electron subsystem at 2T- and 1T-stages. In Fig. 22, these regions are approximated by straight lines. As follows from Fig. 22, the duration of the 2T stage increases with increasing pulse energy. In addition, the slope of the dependences increases with increasing energy at the 1T stage.

10. TWO-TEMPERATURE HEAT CONDUCTION THEORY

The theoretical dependence of the thermal conductivity coefficient κ is found by adding the electron-electron and electron-phonon thermal resistances $1/\kappa$. The theory of electron-electron scattering is described in [41]. Here, this theory is modified to the case of gold. We calculate the thermal conductivity coefficient in the case of only electron-phonon interaction, κ_{ei}, in accordance with the recent work [42]. Note that in [42] electron-electron scattering is not taken into account. Our approach is suitable in both 2T and 1T states. In the solid phase in the 1T state at temperatures above the Debye temperature, the values of our coefficient κ correspond to the known tabular values.

In the 2T state, $T_e \gg T_i$, the main contribution to the electronic thermal conductivity is the thermal conductivity due to electron-electron collisions. We calculated the heat conduction coefficient κ_{ee} due to electron-electron collisions, as done in [41], using the kinetic equation for electrons. In the case of gold, the κ_{ee} coefficient consists of the sum of two summands: κ_{ss} and κ_{sd}. They correspond to the contribution of s–s- and s–d- electron scattering to the heat transfer coefficient. The values κ_{ss} and κ_{sd} according to Drude's formula determine the corresponding average frequencies ν_{ss}, ν_{sd} of s–s- and s–d- scattering.

The solution of the kinetic equation is found in the relaxation time approximation. The approximation of this solution as the sum of separately calculated κ_{ss} and κ_{sd} in the case of gold [48] has the following form

$$\kappa_{ee}^{-1}(T_e,x) = \frac{9.294\cdot 10^{-4}(t/x)}{1+0.03\sqrt{t}-0.2688t+0.9722t^2}. \quad (14)$$

Formula (14) gives the values of the coefficient κ_{ee} in SI units: W/K/m. Here we have introduced the reduced density

$$x = \rho / \rho_0 \quad (15)$$

with $\rho_0 = 19.5$ g/cm^3 and dimensionless electron temperature

$$t = 0.0000561977 T_e/x. \quad (16)$$

As stated, in our approach the heat transfer coefficient κ_{ei} for electron-phonon scattering at normal density is taken according to [42]. Taking into account the density dependence, the coefficient κ_{ei} can be approximated by the expression

$$\kappa_{ei}(T_e,T_i,x) = 21857t\frac{1-1.82427t+2.22019t^2}{1-1.14826t+6.72599t^2}\times \times x^{4/3}y(x)\frac{300}{T_i}. \quad (17)$$

The value of κ_{ei} in this expression, as in formula (14) above, is given in SI units. The ionic temperature T_i is given in Kelvin degrees.

In formula (17), the dimensionless function defined below is introduced

$$y(x) = \frac{1.1963x^{4.6932}}{1+0.196302x^{2.8466}},$$

which takes into account the dependence of the Debye temperature on the density.

Taking into account both electron-ion (17) and electron-electron (14) scattering, the heat transfer coefficient is written in the following form:

$$\kappa(T_e,T_i,x) = \left(k_e\kappa_{ee}^{-1}(T_e,x)+\kappa_{ei}^{-1}(T_e,T_i,x)^{-1}\right)^{-1}. \quad (18)$$

In expression (18), we kept the dimensionless factor k_e, to be able to vary the electron-electron contribution to the heat transfer coefficient.

Formula (18) is applied in the preceding Sects. 2-7. An example of calculation of the coefficient κ is given above in Fig. 2 and 10. It follows from Fig. 2 that in 1T states at temperatures below the melting point of gold, the coefficient (18) reaches the tabulated values of $\kappa \approx 300$ W/K/m.

The calculation of thermal conductivity is an important component in modeling laser exposure using the 2T code.

11. OPTICAL MODEL

The 2T code used above transforms the initial data into dependences $T_e(x, t)$, $T_i(x, t)$. The initial data are the values of the absorbed energy F_{abs} and pulse duration τ_L taken from the experiment (of course, with predetermined dependences of the coefficients κ and α on the parameters describing the state of gold). Together with the functions $T_e(x, t)$, $T_i(x, t)$, the time dependences of surface temperatures are determined: $T_e|_{surf}(t)$, $T_i|_{surf}(t)$, see the example in Fig. 7 above. To recalculate the evolution of surface temperatures into a time-dependent TTR dependence, we use the optical model below. Theoretically calculated TTR time dependencies are compared with the time dependences of TTR from the experiment, see Fig. 16 and 17.

In the Drude-Lorentz approximation, the real and imaginary parts of the dielectric permittivity can be written respectively in the form

$$\varepsilon_1(\omega) = 1 - \frac{\omega_{ps}^2}{\omega^2 + \nu_s^2} + \frac{\omega_{pd}^2(\omega_d^2 - \omega^2)}{(\omega_d^2 - \omega^2)^2 + \omega^2\nu_d^2},$$
$$\varepsilon_2(\omega) = \frac{\omega_{ps}^2}{\omega^2 + \nu_s^2}\frac{\nu_s}{\omega} + \frac{\omega_{pd}^2\omega\nu_d}{(\omega_d^2 - \omega^2)^2 + \omega^2\nu_d^2}.$$

We consider that the frequencies ω_d and ν_d belong to the d zone, where ω is the laser frequency. The plasma frequencies ω_{ps}^2 and ω_{pd}^2 are proportional to the density and contain also the oscillator forces. We explicitly emphasize the proportionality of ω_{ps}^2 and ω_{pd}^2 to the reduced density x:

$$\omega_{ps}^2 = \omega_{0s}^2 x, \quad \omega_{pd}^2 = \omega_{0d}^2 x,$$

the value of x is defined by formula (15), with the index zero emphasizing the values of frequencies at normal density $x = 1$. For the small emission frequencies ω ($\lambda = 800$ nm, far from the edge of the d-zone of gold, probe-pulse) that we consider:

$$\varepsilon_1(\omega) = 1 - \frac{\omega_{0s}^2 x}{\omega^2 + \nu_s^2} + \frac{\omega_{0d}^2 x}{\omega_d^2},$$
$$\varepsilon_2(\omega) = \frac{\omega_{0s}^2 x}{\omega^2 + \nu_s^2}\frac{\nu_s}{\omega} + \frac{\omega_{0d}^2\nu_d}{\omega_d^4}\omega x.$$

In the Drude-Lorentz approximation from the d-zone there remain the additive summands – these are the last summands in the above two formulas. By these additions the Drude-Lorentz model differs from the Drude model in the case when the photon energy is essentially less than the energy of the d-zone edge.

Considering the values of ω_{0d}, ω_d, ν_d constant and introducing constant values b_1, b_2, we get

$$\varepsilon_1(\omega) = 1 - \frac{\omega_{0s}^2 x}{\omega^2 + \nu_s^2} + b_1 x,$$
$$\varepsilon_2(\omega) = \frac{\omega_{0s}^2 x}{\omega^2 + \nu_s^2}\frac{\nu_s}{\omega} + b_2\omega x.$$

Under normal conditions ($x = 1$, $T_i = T_{rt} = 293$ K, T_{rt} is room temperature), we denote the relaxation frequency ν_s by ν_{s0}. Let us use the dielectric constants known for the two frequencies ω_1 and ω_2 from [60]. As a result, we obtain four equations for four unknown quantities, $\omega^2{}_{0s}$, ν_{s0}, b_1, b_2:

$$\varepsilon_1(\omega_1) = 1 - \frac{\omega_{0s}^2}{\omega_1^2 + \nu_{s0}^2} + b_1,$$
$$\varepsilon_2(\omega_1) = \frac{\omega_{0s}^2}{\omega_1^2 + \nu_{s0}^2}\frac{\nu_{s0}}{\omega_1} + b_2\omega_1,$$
$$\varepsilon_1(\omega_2) = 1 - \frac{\omega_{0s}^2}{\omega_2^2 + \nu_{s0}^2} + b_1,$$
$$\varepsilon_2(\omega_2) = \frac{\omega_{0s}^2}{\omega_2^2 + \nu_{s0}^2}\frac{\nu_{s0}}{\omega_2} + b_2\omega_2.$$

From this system of the equations, we obtain a cubic equation for the value of $\xi = \nu_{s0}/\omega_1$:

$$\xi\left(1 + \left(\frac{\omega_2}{\omega_1}\right)^2 + \xi^2\right) = -\frac{\varepsilon_2(\omega_1)\dfrac{\omega_2}{\omega_1} - \varepsilon_2(\omega_2)}{\varepsilon_1(\omega_1) - \varepsilon_1(\omega_2)}\frac{\omega_2}{\omega_1}.$$

Solving this equation, we find ξ, and hence ν_{s0}. Then we find the three quantities we need $\omega^2{}_{0s}$, b_1, b_2:

$$\frac{\omega_{0s}^2}{\omega_1^2} = \frac{\varepsilon_1(\omega_1) - \varepsilon_1(\omega_2)}{\left((\omega_2/\omega_1)^2 + \xi^2\right)^{-1} - \left(1 + \xi^2\right)^{-1}},$$
$$b_1 = \varepsilon_1(\omega_1) - 1 + \frac{\omega_{0s}^2}{\omega_1^2}\left(1 + \xi^2\right)^{-1},$$
$$b_2\omega_1 = \varepsilon_2(\omega_1) - \frac{\omega_{0s}^2}{\omega_1^2}\left(1 + \xi^2\right)^{-1}\xi.$$

Let us take two frequency lines corresponding to the wavelengths $\lambda_1 = 800$ nm and $\lambda_2 = 1800$ nm.

From [60] for the case of gold under consideration we have taken the values of

$$\varepsilon_1(\omega_1) = -23.360, \quad \varepsilon_2(\omega_1) = 0.76850,$$

$$\varepsilon_1(\omega_2) = -147.20, \quad \varepsilon_2(\omega_2) = 5.4235.$$

It results

$$\xi = 0.01523, \quad \nu_{s0} = 0.03588 \cdot 10^{15}\,\mathrm{s}^{-1},$$

$$\omega_{0s}^2 / \omega_1^2 = 30.5266, \quad b_1 = 6.1595, \quad b_2\omega_1 = 0.3038.$$

In the 2T state, the relaxation frequency ν_s is the sum of the frequencies of electron-phonon s–i- and electron-electron s–s- and s–d- collisions:

$$\nu_s(T_e, T_i, x) =$$

$$= \nu_{si}(T_i, x) + A_{ss}\nu_{ss}(T_e, x) + A_{sd}\nu_{sd}(T_e, x).$$

Here $A_{ss} \sim 1$, $A_{sd} \approx 1$ are tuning parameters. They are selected so that the maxima of experimental and theoretical TTR-dependences were the same – normalization to the maximum.

The frequency ν_{si} is expressed through ν_{s0} as

$$\nu_{si}(T_i, x) = \nu_{s0}\frac{x}{x_0}\frac{y(x_0)}{y(x)}\frac{2/5 + T_i/\Theta(x)}{2/5 + T_r/\Theta(x)}.$$

Here we introduce the function

$$y(x) = \frac{x^{2a+1}}{b + 1 + (a - b)\,x^{a+1}}$$

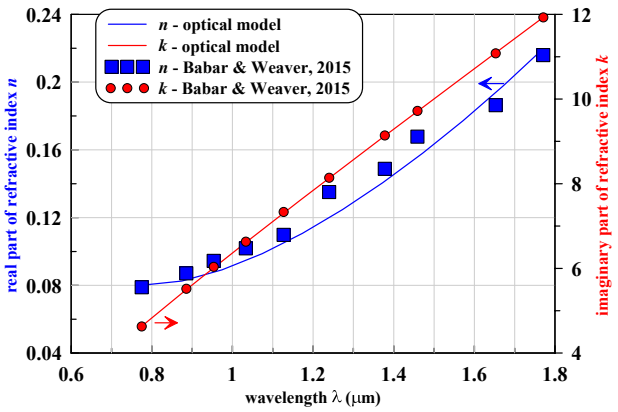

Fig. 23. (In color online) The real (n, blue symbols and curve) and imaginary (k, red symbols and curve) parts of the refractive index $n + ik$ of gold as a function of wavelength. The symbols are the data from [60], solid curves are refractive index $n + ik$, corresponding to the dielectric permittivity in the form (19) and (20).

and the Debye temperature depending on the reduced density x

$$\Theta(x) = \Theta_0\left(\frac{x}{x_0}\right)^{1/3}\sqrt{\frac{y(x)}{y(x_0)}}.$$

In this expression, $\Theta_0 = 170$ K is the Debye temperature at a density of 19.3 g/cm^3, $a = 3.92$ and $b = 1.95$ are degree exponents in the expression $p(x) = p_0(x^{a+1} - x^{b+1})$, which approximates the so-called cold pressure (pressure-density dependence at zero temperature).

The frequencies ν_{ss} and ν_{sd} were calculated together with the calculation of the corresponding heat transfer coefficients κ_{ss} and κ_{sd} and can be represented by the following approximating relationships:

$$\nu_{ss}(T_e, x) = 1.13845\frac{x}{x_0}t^2\frac{1 + 0.784364t^2}{1 + 0.656757t^{3.11359}}10^{15}\,\mathrm{s}^{-1}$$

and

$$\nu_{sd}(T_e, x) = 2.7956\frac{x}{x_0}e^{-\frac{2.6047}{t}}\frac{1 + 3.4355t^{1.6311}}{1 + 1.3559t^{1.8054}}10^{15}\,\mathrm{s}^{-1},$$

where the dimensionless electron temperature t is determined by normalization (16).

In the 2T-state the real and imaginary parts of the dielectric permittivity are equal to

$$\varepsilon_1(\omega, T_e, T_i, x) = 1 - \frac{\omega_{0s}^2 x}{\omega^2 + \nu_s^2(T_e, T_i, x)} + b_1 x \quad (19)$$

$$\varepsilon_2(\omega, T_e, T_i, x) = \frac{\omega_{0s}^2 x}{\omega^2 + \nu_s^2(T_e, T_i, x)}\frac{\nu_s(T_e, T_i, x}{\omega} + b_2\omega x. \quad (20)$$

They determine the complex refractive index of a gold film of thickness H_2:

$$n_2 = \left(\frac{\sqrt{\varepsilon_1^2 + \varepsilon_2^2} + \varepsilon_1}{2}\right)^{1/2} + i\left(\frac{\sqrt{\varepsilon_1^2 + \varepsilon_2^2} - \varepsilon_1}{2}\right)^{1/2}.$$

The real (n) and imaginary (k) parts of the refractive index of gold as a function of wavelength in the wavelength range of interest to us are shown in Fig. 23. The symbols show the data of [60], and the solid curves show the calculation according to the optical model given in this chapter.

The multilayer structure we consider consists of vacuum, in which the wave number of the probing pulse $k_1 = 2\pi/\lambda$, a gold film of thickness H_2, in which

the wave number $k_2 = k_1 n_2$, a glass substrate of thickness H_3, in which the wave number $k_3 = k_1 n_3$ ($n_3 = 1.5$), and vacuum again. Let us introduce for such a structure the values A and B of the following form:

$$A = \left(1 - \frac{k_2}{k_1}\right) e^{-ik_2 H_2} \left[\begin{array}{l} \left(1 + \frac{k_3}{k_2}\right)\left(1 + \frac{k_4}{k_3}\right) e^{-ik_3 H_3} + \\ + \left(1 - \frac{k_3}{k_2}\right)\left(1 - \frac{k_4}{k_3}\right) e^{ik_3 H_3} \end{array} \right] +$$

$$+ \left(1 + \frac{k_2}{k_1}\right) e^{ik_2 H_2} \left[\begin{array}{l} \left(1 - \frac{k_3}{k_2}\right)\left(1 + \frac{k_4}{k_3}\right) e^{-ik_3 H_3} + \\ + \left(1 + \frac{k_3}{k_2}\right)\left(1 - \frac{k_4}{k_3}\right) e^{ik_3 H_3} \end{array} \right],$$

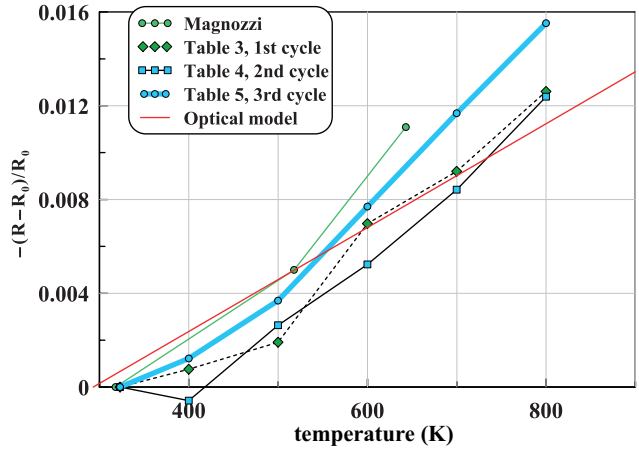

Fig. 24. (In color online) Comparison of the calculation by our optical model with the data of [61, 62]. The green curve with green round signs is taken from the paper [62]. The curves in Tables 3, 4, and 5 are taken from these tables in [61]. The dependence shown by the red line represents our model in the 1T case.

$$B = \left(1 + \frac{k_2}{k_1}\right) e^{-ik_2 H_2} \left[\begin{array}{l} (1 + \frac{k_3}{k_2})(1 + \frac{k_4}{k_3}) e^{-ik_3 H_3} + \\ + (1 - \frac{k_3}{k_2})(1 - \frac{k_4}{k_3}) e^{ik_3 H_3} \end{array} \right] +$$

$$+ \left(1 - \frac{k_2}{k_1}\right) e^{ik_2 H_2} \left[\begin{array}{l} \left(1 - \frac{k_3}{k_2}\right)\left(1 + \frac{k_4}{k_3}\right) e^{-ik_3 H_3} + \\ + \left(1 + \frac{k_3}{k_2}\right)\left(1 - \frac{k_4}{k_3}\right) e^{ik_3 H_3} \end{array} \right].$$

The described optical model was used to transform the 2T-code data into a time dependence of TTR. This dependence is shown in Fig. 15 and 16.

To verify the model, we used literature data – works [61, 62]. They studied changes in the reflectivity of gold upon heating. This is necessary for applications in plasmonics. Fig. 24 shows a comparison of the developed optical model with the results of [61, 62]. The optical characteristics were calculated in 1T states with one temperature $T_e = T_i$. This temperature is plotted on the abscissa axis in Fig. 24. As can be seen, there is a satisfactory agreement.

The results presented in Fig. 24 are important for understanding the dependences of α and κ. Let us try to explain why.

As shown above (see Sects. 5-7), at the pronounced 2T stage, the cooling of the bulk target surface is mainly carried out by electronic heat conduction. We needed to decrease the coefficient κ to achieve agreement with experiment in the rate of decline of the electronic temperature of the surface. Then, if we use the known theoretical values for the coefficient α (i.e., sufficiently high values), we obtain high values for the ionic temperature at the transition from the 2T- to 1T-stage.

The point is that at small coefficients κ the heating layer turns out to be thin. The absorbed energy is concentrated in it. And the temperature of this layer at the 1T stage becomes high. This follows from the law of conservation of energy. The product of the thickness of the heating layer by its temperature is proportional to the absorbed energy. To reduce the ionic temperature at the transition from 2T- to 1T-stage, it is necessary to reduce the coefficient α significantly below the theoretical values, see Fig. 17.

From the above, it is clear how important it is to accurately determine the surface temperature from the experimentally measured TTR dependence at the transition to the 1T stage. Therefore, it was necessary to compare our model with 1T experiments to be sure of this. Such a comparison is presented in Fig. 24.

12. CONCLUSION

The work is based on an experiment. In the presented experiment, the lock-in technique was modified in order to measure the TTR signal at the highest possible absorbed energies. Reducing the frequency in the lock-in technique to 31 Hz allowed the bulk gold targets to rise to temperatures close to the melting point of gold. In previous experiments, the limiting temperatures in the lock-in technique were significantly lower.

The experimental results obtained represent measurements of the reflectivity of gold after irradiation of the target with fs-pulse. Undoubtedly, these TTR measurements are indirect evidence of 2T-relaxation processes occurring in the target substance. The interpretation of these measurements is of scientific value.

The interpretation requires a theoretical model and numerical modeling based on this model. Such a model was created and calculations were carried out. There are two most important characteristics of 2T states. They are the heat transfer coefficient κ and the coefficient α, which determines the rate of energy exchange between the electron and ionic subsystems.

Through this paper, the following circumstances have been clarified.

In bulk targets in the whole range of laser fs-pulse energies investigated, the rate of decrease of the electronic temperature of the surface at the 2T stage is determined by the electronic transport of the absorbed energy. At the same time, the surface cooling due to the α coefficient takes place, but plays a minor role. The maximum electronic temperature was about 20 kK.

It is shown that in the range of maximum electron temperatures 10-20 kK there is a significant decrease in the electron thermal conductivity coefficient κ compared to its value in the developed theory. At lower temperatures, the theoretical coefficient κ describes the situation well.

From the treatment of the experiments, a similar conclusion is drawn concerning the coefficient α. In the range of maximum electron temperatures 10-20 kK the coefficient α is much smaller than the values following from the existing theories. At low temperatures T_e the coefficient α returns to the theoretical values.

The return of the coefficient α to rather large theoretical values at low temperatures T_e, i.e., at the 1T stage, allows us to describe the slow temperature decrease in experiments at the 1T stage in a long-time interval (hundreds of picoseconds). At underestimated values of the coefficient α, the rate of temperature decreases over a long time interval is too small.

FUNDING

This work was supported by the Russian Science Foundation (grant No. 19-19-00697-P, extended).

REFERENCES

1. A.B. Cherepakhin, D. V. Pavlov, I. I. Shishkin et al., *Appl. Phys. Lett.* **117**, 041108 (2020).
2. S. I. Kudryashov, A. A. Samokhvalov, Ya. D. Golubev et al., *Appl. Surf. Sci.* **537**, 147940 (2021).
3. K. Kaleris, E. Kaniolakis-Kaloudis, E. Kaselouris et al., *Appl. Phys. A* **129**, 527 (2023).
4. S. A. Romashevskiy, A. I. Ignatov, V. V. Zhakhovsky et al., *Appl. Surf. Sci.* **615**, 156212 (2023).
5. T. Kawashima, T. Sano, A. Hirose et al., *J. Mater. Process.Technol.* **262**, 111 (2018).
6. U. Trdan, T. Sano, D. Klobcar et al., *Corrosion Sci.* **143**, 46 (2018).
7. N. A. Inogamov, E. A. Perov, V. V. Zhakhovsky et al., *JETP Lett.* **115**, 71 (2022).
8. V. A. Khokhlov, V. V. Zhakhovsky, N. A. Inogamov et al., *JETP Lett.* **115**, 523 (2022).
9. V. Zhakhovsky, Yu. Kolobov, S. Ashitkov et al., *Phys. Fluids* **35**, 096104 (2023).
10. S. I. Anisimov, B. L. Kapeliovich, and T. L. Perel'man, *Sov. Phys. JETP* **39**, 375 (1974).
11. W. S. Fann, R. Storz, H. W. K. Tom, and J. Bokor, *Phys. Rev. Lett.* **68**, 2834 (1992).
12. C.-K. Sun, F. Vall'ee, L. H. Acioli et al., *Phys. Rev. B* **50**, 15337 (1994).
13. J. Hohlfeld, S.-S. Wellershoff, J. Guedde et al., *Chem. Phys.* **251**, 237 (2000).
14. N. Del Fatti, C. Voisin, M. Achermann et al., *Phys. Rev. B* **61**, 16956 (2000).
15. A. N. Smith and P. M. Norris, *Appl. Phys. Lett.* **78**, 1240 (2001).
16. P. E. Hopkins, J. M. Klopf, and P. M. Norris, *Appl. Opt.* **46**, 2076 (2007).
17. Yu. V. Petrov, K. P. Migdal, N. A. Inogamov, and V. V. Zhakhovsky, *Appl. Phys. B* **119**, 401 (2015).
18. Yu. V. Petrov, K. P. Migdal, N. A. Inogamov, and S. I. Anisimov, *JETP Lett.* **104**, 431 (2016).
19. B.Y. Mueller and B. Rethfeld, *Phys. Rev. B* **87**, 035139 (2013).
20. B. Rethfeld, D. S. Ivanov, M. E. Garcia, and S. I. Anisimov, *J. Phys. D* **50**, 193001 (2017).
21. A. A. Abrikosov, *Fundamentals of the Theory of Metals*, Moscow, Nauka (1987).
22. S. Chapman and T. G. Cowling, *The Mathematical Theory of Non-Uniform Gases*, Cambridge Univ. Press (1970).
23. M. I. Kaganov, I. M. Lifshitz, and L. V. Tanatarov, *Sov. Phys. JETP* **4**(2), 173 (1957).
24. Yu. V. Petrov, *Laser Part. Beams* **23**, 283 (2005).
25. V. V. Temnov, K. Sokolowski-Tinten, P. Zhou, and D. von der Linde, *J. Opt. Soc. Am. B* **23**, 1954 (2006).
26. C. A. Paddock and G. L. Eesley, *J. Appl. Phys.* **60**, 285 (1986).
27. N. A. Inogamov, V. A. Khokhlov, S. A. Romashevskiy et al., *JETP Lett.* **117**, 104 (2023).
28. V. V. Temnov, C. Klieber, K. A. Nelson et al., *Nature Commun.* **4**, 1468 (2013).
29. F. Akhmetov, I. Milov, S. Semin et al., *Vacuum* **212**, 112045 (2023).

30. K. Sokolowski-Tinten, J. Bialkowski, A. Cavalleri et al., *Phys. Rev. Lett.* **81**, 224 (1998).
31. N. A. Inogamov, V. V. Zhakhovskii, S. I. Ashitkov et al., *JETP* **107**, 1 (2008).
32. J. C. Crowhurst, M. R. Armstrong, K. B. Knight et al., *Phys. Rev. Lett.* **107**, 144302 (2011).
33. S. I. Ashitkov, P. S. Komarov, M. B. Agranat et al., *JETP Lett.* **98**, 384 (2013).
34. N. Hasegawa, M. Nishikino, M. Ishino et al., *Springer Proc. Phys.* **202**, 273 (2018).
35. B. Albertazzi, N. Ozaki, V. Zhakhovsky et al., *Sci. Adv.* **3**, e160270 (2017).
36. M. Z. Mo, Z. Chen, R. K. Li et al., *Science* **360** (6396), 1451 (2018).
37. R. Fang, A. Vorobyev, and Ch. Guo, *Light*: *Sci. Appl.* **6**, e16256 (2017).
38. N. A. Inogamov, A. M. Oparin, Yu. V. Petrov et al., *JETP Lett.* **69**, 310 (1999).
39. V. V. Zhakhovskii, K. Nishihara, S. I. Anisimov, and N. A. Inogamov, *JETP Lett.* **71**, 167 (2000).
40. L. V. Zhigilei and B. J. Garrison, *J. Appl. Phys.* **88**, 1281 (2000).
41. N. A. Inogamov and Yu. V. Petrov, *JETP* **110**, 446 (2010).
42. N. A. Smirnov, *Phys. Rev. B* **106**, 024109 (2022).
43. Zh. Lin, L. V. Zhigilei, and V. Celli, *Phys. Rev. B* **77**, 075133 (2008).
44. N. A. Inogamov, V. V. Zhakhovskii, and V. A. Khokhlov, *JETP* **120**, 15 (2015).
45. S. I. Anisimov, V. V. Zhakhovsky, N. A. Inogamov et al., *JETP* **129**, 757 (2019)].
46. M. E. Povarnitsyn, T. E. Itina, P. R. Levashov, and K. V. Khishchenko, *Phys. Chem. Chem. Phys.* **15**, 3108 (2013).
47. A. Block, R. Yu, Ieng-Wai Un et al., *ACS Photonics* **10**, 1150 (2023).
48. Yu. V. Petrov, N. A. Inogamov, and K.P. Migdal, *JETP Lett.* **97**, 20 (2013).
49. S. I. Ashitkov, P. S. Komarov, V. V. Zhakhovsky et al., *J. Phys.*: *Conf. Ser.* **774**, 012097 (2016).
50. A. Block, M. Liebel, R. Yu et al., *Sci. Adv.* **5**, eaav8965 (2019).
51. M. Segovia and X. Xu, *Nano Lett.* **21**, 7228 (2021).
52. G. Gao, L. Jiang, B. Xue et al., *Small Methods* **7**, 2201260 (2023).
53. N. A. Inogamov, V. V. Zhakhovsky, S. I. Ashitkov et al., *Contrib. Plasma Phys.* **51**, 367 (2011).
54. N. A. Inogamov and V. V. Zhakhovsky, *J. Phys.*: *Conf. Ser.* **681**, 012001 (2016).
55. N. A. Inogamov, V. V. Zhakhovsky, V. A. Khokhlov et al., *J. Phys.*: *Conf. Ser.* **774**, 012102 (2016).
56. V. V. Shepelev and N. A. Inogamov, *J. Phys*: *Conf. Ser.* **946**, 012010 (2018).
57. J. M. Liu, *Opt. Lett.* **7**, 196 (1982).
58. S. I. Kudryashov, A. A. Samokhvalov, Ya. D. Golubev et al., *Appl. Surf. Sci.* **537**, 147940 (2021).
59. S. I. Ashitkov, N. A. Inogamov, P. S. Komarov et al., *High Temp.* **60**, 192 (2022).
60. S. Babar and J. H. Weaver, *Appl. Opt.* **54**, 477 (2015).
61. H. Reddy, U. Guler, A. V. Kildishev et al., *Opt. Mater. Express* **6**, 2776 (2016).
62. M. Magnozzi, M. Ferrera, L. Mattera et al., *Nanoscale* **11**, 1140 (2019).